Universidade de Aveiro Departamento de Física,
2015

Filipe Daniel Rodrigues Santos

Campos magnéticos críticos em sistemas supercondutores com bandas semi-metálicas

Critical magnetic fields in superconducting systems with semi-metallic bands

Universidade de Aveiro Departamento de Física,
2015

Filipe Daniel Rodrigues Santos

Campos magnéticos críticos em sistemas supercondutores com bandas semi-metálicas

Critical magnetic fields in superconducting systems with semi-metallic bands

Dissertation presented at the University of Aveiro for the fulfilling of the requirements for obtaining the Master's degree in Physics, supervised by Dr. R. Dias, assistant professor from the Department of Physics of the University of Aveiro.

the jury

president	**Dr. Manuel António dos Santos Barroso** Assistant professor of the University of Aveiro
examiners committee	**Dr. Ricardo Assis Guimarães Dias** Assistant professor of the University of Aveiro
	Dr. Eduardo Filipe Vieira de Castro Assistant professor at the IST of the University of Lisbon

acknowledgements

I take this opportunity to express my appreciation to my supervisor Dr. R. Dias for his exemplary guidance and constant encouragement throughout the course of this thesis. I also would like to offer my thanks to my family and my friends for their support throughout my academic path.

keywords superconductivity, BCS theory, Zeeman splitting effects, metastability region, critical intraband interaction, graphene, GIC's, semi-metal, orbital effects, pair propagator, upper critical fields

abstract In this work, we study the Zeeman splitting effects in the parallel magnetic field versus temperature phase diagram of two-dimensional superconductors with one graphene-like band and the orbital effects of perpendicular magnetic fields in isotropic two-dimensional semi-metallic superconductors. We show that when parallel magnetic fields are applied to graphene and as the intraband interaction decreases to a critical value, the width of the metastability region present in the phase diagram decreases, vanishing completely at that critical value. In the case of two-band superconductors with one graphene-like band, a new critical interaction, associated primarily with the graphene-like band, is required in order for a second metastability region to be present in the phase diagram. For intermediate values of this interaction, a low-temperature first-order transition line bifurcates at an intermediate temperature into a first-order transition between superconducting phases and a second-order transition line between the normal and the superconducting states. In our study on the upper critical fields in generic semi-metallic superconductors, we find that the pair propagator decays faster than that of a superconductor with a metallic band. As result, the zero field band gap equation does not have solution for weak intraband interactions, meaning that there is a critical intraband interaction value in order for a superconducting phase to be present in semi-metallic superconductors. Finally, we show that the out-of-plane critical magnetic field versus temperature phase diagram displays a positive curvature, contrasting with the parabolic-like behaviour typical of metallic superconductors.

palavras-chave

supercondutividade, teoria BCS, efeito de Zeeman, região de metastabilidade, interação crítica de banda, grafeno, GIC's, semi-metal, efeitos orbitais, propagador de pares, campos críticos

resumo

Neste trabalho, estudamos o efeito de Zeeman nos diagramas de fases do campo magnético versus temperatura de supercondutores bidimensionais com uma banda de grafeno na sua composição, sobre a ação de campos magnéticos paralelos e os efeitos orbitais em supercondutores semi-metálicos bidimensionais e isotrópicos sobre a ação de campos magnéticos perpendiculares. Mostramos que quando se aplica campos magnéticos paralelamente a uma camada de grafeno e à medida que a interação da banda diminui, a largura da zona de metastabilidade presente no diagrama de fases diminui, desaparecendo por completo quando a interação toma um valor crítico. No caso de supercondutors de duas bandas com uma banda de grafeno, existe uma nova interação crítica, associada principalmente à banda de grafeno, necessária ao surgimento de uma segunda zona de metastabilidade no diagrama de fases. Para valores intermédios dessa interação, a transição de primeira ordem que surge, no diagrama de fases, a baixas temperaturas, ramifica-se, a temperaturas intermedias, numa transição de primeira ordem entre fases supercondutoras e numa transição de segunda ordem entre os estados não supercondutor e supercondutor. Em relação ao nosso estudo, sobre os efeitos orbitais em supercondutores semi-metálicos genéricos, descubrimos que o propagador de pares decai, com a distância, mais depressa do que no caso de um supercondutor metálico. Como consequência, a equação de *gap* a campo nulo não tem solução para fracas interações da banda semi-metálica indicando a existência de um valor crítico para a interação da banda necessária à existência de uma fase supercondutora em supercondutores semi-metálicos. Mostramos finalmente que o diagrama de fases do campo crítico magnético versus temperatura exibe uma curvatura positiva em contraste com a curva parabólica do diagrama de fases típico de supercondutores metálicos.

Contents

List of Figures

Chapter 1

Introduction

Graphene, a one-atom thick layer of graphite, is a two-dimensional gapless semi-metal recently (2004) isolated from graphite, for the first time by Andre Geim and Konstantin Novoselov [1]. It is at the same time the thinnest and the strongest known material in the universe, shows a large thermal conductivity and can sustain current densities six orders of magnitude higher than that of copper [2]. However, what caught the attention of physicists were unusual phenomena like the anomalous quantization of the Hall conductance and the weak-localization, which deviated from the well-established theory of electronic transport in two-dimensional systems [3, 4]. It is now known that at low temperatures, the charge carriers of graphene behave as massless chiral relativistic particles [3] and thus, its dynamics is not described by the standard Schrodinger equation but instead by the relativistic Dirac equation for massless particles [4]. In spite of its interesting electrical properties, superconductivity is unlikely to be observed in isolated graphene, due to its low dimensionality and resulting enhanced fluctuations, but also due to the semi-metallic nature of graphene [5]. In fact, using a simple BCS mean-field approach, one concludes that a critical pairing interaction is required in order for a superconducting phase to be present in graphene [5]. However, when doped, the Fermi energy of graphene shifts away from the Dirac point, where the density of states (DOS) vanishes, and the finite DOS at the Fermi energy leads to a finite superconducting critical temperature for arbitrarily small attractive pairing potentials [5]. One should note that the absence of superconductivity in undoped graphene stated by the Mermin-Wagner theorem is in apparent contradiction with the mean-field approach. This theorem states that in materials with $D \leqslant 2$ (in which D represents the dimensionality of a material), which is the case of graphene, long-range fluctuations can be created with little energy cost [6, 7]. The appearance of such fluctuations decreases the chances of observing superconducting-like properties in strictly 2D materials. However, superconductivity in graphene is possible in tridimensional graphene based structures.

A way of inducing superconductivity in graphene is by proximity effect in S-G-S structures [8] (two superconducting metals connected to a graphene sheet). These systems are analogous to a two-band superconductor system (with no intraband interactions in one of the bands) since the Josephson tunneling can be interpreted as an interband interaction [9, 10, 11]. Another way of inducing superconductivity in graphene is by intercalation of graphene sheets with metallic sheets. In graphite intercalation compounds (GICs) superconductivity in known to be present for

almost half a century [12], being successfully observed in recent works [13, 14, 15]. There has been a strong debate in the last decades about whether GICs are one-band (due to the metallic interlayer band [16] or due to the graphene-like band [17]) or two-band superconductors (a graphene-like band and a metallic interlayer band) [18, 19, 20, 21, 22, 23, 24, 25]. Recent high resolution ARPES measurements, performed on CaC_6, present strong evidence supporting the scenario of both bands contributing to the superconducting phase [26]. The motivation for this work is largely due to the expectations created from these results.

In this work we present a study of the phase diagram of one-band and two-band 2D superconductors with one semi-metallic band. In particular, we study: **i)** Zeeman splitting effects in one- and two-band graphene based superconductors; **ii)** the upper critical field, due to orbital effects of perpendicular magnetic fields, in generic superconducting semi-metals.

In our study of in-plane critical magnetic fields [point **i)**], we carry out a study of metastability regions in the phase diagram of superconducting graphene and intercalated graphite superconductors under in-plane magnetic fields, using a weak coupling BCS approach. We consider only stage-2 GICs in our study since these compounds present a very high anisotropy, suggesting that they can be considered quasi-2D materials and thus allowing us, due to their reduced dimensionality, to neglect the orbital effect of the magnetic field (which becomes strongly attenuated as one moves away from the critical temperature T_c, with decreasing temperature) and to consider the Zeeman effect the dominant one. The degree of anisotropy in GICs can be measured by the critical magnetic field anisotropy ratio $\Gamma_H = H_c^{\parallel}/H_c^{\perp}$ [27], where $H_c^{\parallel}$ ($H_c^{\perp}$) is the critical magnetic field when applied parallel (perpendicular) to the graphene sheets. The range of values for Γ_H differs greatly from stage-1 to stage-2 GICs. Stage-1 compounds have been reported to have $\Gamma_H \sim 2-11$ [28, 15], whereas in stage-2 compounds Γ_H can have values that go up to 40 [28].

In order to understand the new behavior due to the semi-metallic graphene-like band, we reproduce the band gap solutions and the in-plane magnetic field *vs.* temperature phase diagram of quasi-2D n-band metal based superconductors, which have been known for some time [29, 30, 31], and compare these results to the ones of graphene based superconductors. We find that, due to the vanishing density of states at the Dirac point of graphene, and in contrast to what happens in metallic superconductors, the width of the metastability region associated with the low temperature first-order transition (FOT) to the normal phase (normalized to the zero temperature critical field) shows a strong dependence on doping, vanishing at zero doping. In the case of intercalated graphite superconductors, modeled as 2D two-band superconductors, we find that a critical pairing interaction is required in order for a second metastability region (associated primarily with the intraband pairing in the graphene-like band) to be present in the in-plane magnetic field *vs.* temperature phase diagram. For intermediate values of the graphene-like intraband interaction above this critical value, a low-temperature FOT bifurcates at intermediate temperature into a FOT between superconducting phases and a second-order transition (SOT) between the normal and the superconducting phase. These features are not exclusive to graphene based superconductors and should also be observed in any quasi-2D superconductor with a semi-metallic band.

In our study of out-of-plane critical magnetic fields [point **ii)**], we study the pair propagator spacial and temperature dependence for a isotropic 2D one-band semi-metallic superconductor.

We find that, due to the vanishing of the semi-metallic density of states at the Fermi energy, the pair propagator of a superconductor with a semi-metallic band decays faster than that of a superconductor with a metallic band. As a result, the zero field band gap equation does not have solution for weak interactions implying that a critical intraband interaction is required in order for a superconducting phase to be present in the case of semi-metallic superconductors. Furthermore, we study the magnetic field *vs.* temperature phase diagram of a semi-metallic superconductor under perpendicular magnetic fields. We find that in contrast with the case of a one-band metallic superconductor, where the phase diagram displays a parabolic transition curve with negative curvature, the temperature dependence of the upper critical field of a semi-metallic superconductor is described by a curve with positive curvature.

This dissertation is divided in 7 chapters, the Introduction being the first one. In chapter 2, we introduce basic superconductivity concepts and present the mathematical formalism which describes it, the BCS theory. We modify the BCS Hamiltonian in order to include a Zeeman term, and derive expressions for the n-band gap solutions for 2D superconductors under parallel magnetic field. In chapter 3, the in-plane magnetic field *vs.* temperature phase diagram for one-band and two-band metallic superconductors is addressed. Next, in chapter 4, we discuss superconductivity in undoped and doped isolated graphene in a mean-field approach. In particular, the notion of critical intraband interaction is covered and the role of doping is discussed. In chapter 5, we address the effects of in-plane magnetic field in the phase diagram of stage-2 GICs. Here, a new notion of critical intraband interaction is introduced and the effects of doping are again addressed. In chapter 6, we derive the n-band gap equations for isotropic 2D superconductors under perpendicular magnetic field and discuss the superconducting upper critical field in one-band metallic and semi-metallic superconductors. Finally, the conclusions of the work, as well suggestions for future work, are reported in chapter 7.

Chapter 2

BCS theory for a n-band superconductor

2.1 Superconductivity

Superconductivity was discovered in 1911 by K. Onnes [32]. In his cooling experiments with mercury, he found that its resistivity suddenly dropped to zero at a temperature $T = 4.2K$ [32]. Below this temperature, denominated transition temperature T_c, [see Fig. 2.1a, top figures], a superconductor differs from a normal metal, mainly, in two properties. A superconductor allows the existence of persistent currents (inside a ring/torus shaped superconductor the current flows forever without any driving voltage, reflecting a zero resistivity) and behaves like a perfect diamagnet, i.e., it expels weak magnetic fields nearly completely from its interior [33]. The latter behaviour, called Meisser effect, is sketched in Fig. 2.1a (bottom diagrams).
In 1950, the transition temperature of mercury was found to vary with the isotopic mass M as $M^{-\frac{1}{2}}$ [33]. This physical phenomenon, called "isotopic effect", confirmed the Frolich's suggestion that the phonon (lattice vibration) modes contribute to superconductivity [33]. Indeed, superconductivity is due to an effective attraction, V, between conduction electrons which leads to the forming of electron pairs. [33]. Although any two electrons feel the Coulomb force which make them repel each other, the effective attraction between electrons can, at extremely low temperatures, overcome the electron repulsion leading them to pair up. This effective interaction is intermediated by an interaction between electrons and the lattice, in which a free electron interacts with the lattice, distorting it, moving its ions slightly toward the electron, and increasing the positive charge density of the lattice in the electron vicinity. A second electron located at the vicinity of this distortion is then attracted to it and consequently towards the first electron [see Fig. 2.1b]. The rigorous quantum mechanical approach explains the pairing of electrons using the electron-phonon interactions concept. In this process, two electrons couple *via* phonon exchange, i.e., an electron attracts the positive ions inside the lattice producing a lattice vibration (i.e. a phonon), that is absorbed by a second electron.

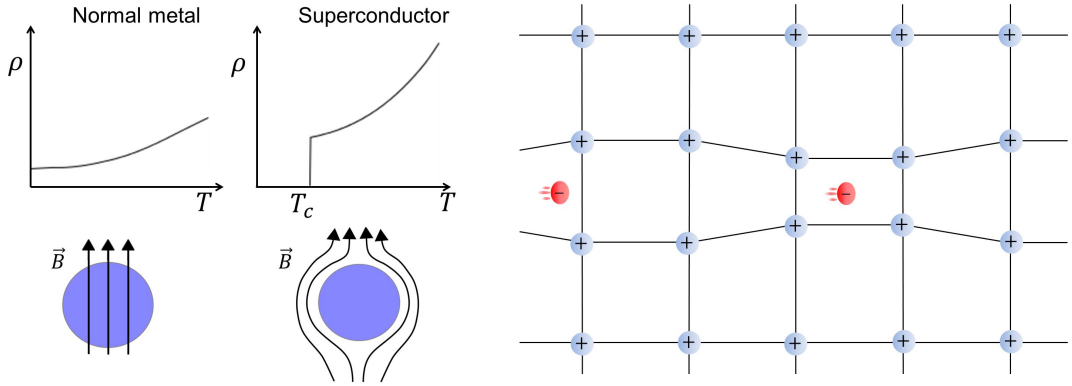

Figure 2.1: (a) Top: Electrical resistivity as a function of temperature, $\rho(T)$. In the case of a superconductor, the resistivity drops to zero at T_c (top right) where in the case of a normal metal it decreases with temperature up to a non zero value at $T = 0$. Bottom: behavior of a normal metal (bottom left) and a superconductor (bottom right) under magnetic fields. The magnetic field expulsion phenomenon (Meisser Effect) only occurs in the case of the superconductor. (b) In a superconducting material, at extremely low temperatures, an electron can pull the positive ions from the lattice towards it, creating a more positive region that attracts a second electron to the area, forming a pair.

2.2 BCS theory

The mathematical formalism that describes these electron pairs, also called Cooper pairs, only arrived in 1957 by Bardeen, Cooper and Schrieffer with the BCS theory (Nobel Prize in 1972) [34]. The BCS theory stated that at sufficiently low temperatures, electrons near the Fermi surface become unstable against the formation of Cooper pairs which occurs in the presence of an attractive potential, no matter how weak. These Cooper pairs form zero-spin bosons, which, due to the large number of these pairs at low temperatures, condense into the same energy level, and thus transport electric current without dissipation.

The required energy to break all the Cooper pairs, which leads to a phase transition from the superconducting to the normal state, is commonly called condensation energy, and is given by $E_c = \frac{1}{2}N(\varepsilon_F)\Delta^2$, where Δ is the superconducting band gap energy. The BCS theory uses a mean-field approach which provides a mathematical relation of Δ with the temperature, T, the intraband interaction, V, and the density of states, $N(\xi)$,

$$\frac{1}{N(\xi)V} = \int_0^{\hbar\omega_c} \frac{\tanh\left(E(\xi,\Delta)/2k_BT\right)}{E(\xi,\Delta)} d\xi, \tag{2.1}$$

where $\hbar$ is the Planck constant, ω_c is the frequency cutoff, and k_B is the Boltzmann constant. $E(\xi,\Delta) = \sqrt{\xi^2+\Delta^2}$ is the quasi-particle energy, where ξ is the energy of the electron in the absence of interactions.

This approach allows one to determine the critical temperature, T_c, and the zero temperature band gap energy, $\Delta(0)$, by doing, respectively, $\Delta = 0$ and $T = 0$ in Eq. 2.1,

$$k_B T_c = 1.13\hbar\omega_c e^{-1/N(0)V}, \tag{2.2}$$

and

$$\Delta_0 = \frac{\hbar\omega_c}{\sinh[1/N(0)V]} \approx 2\hbar\omega_c e^{-1/N(0)V}. \tag{2.3}$$

From Eqs. 2.2 and 2.3 the BCS expression is obtained

$$\frac{2\Delta_0}{k_B T_c} = 3.53. \tag{2.4}$$

Given that the energy gap of a superconductor can be measured in microwave absorption experiments, the BCS prediction and the band gap equation validity can be tested using experimental measurements. In order to do that one can use Rohlf and Blatt data [35, 36] shown in Figs. 2.2a and 2.2b, respectively. The band gap energy and the respective critical temperature are plotted in the Fig. 2.2a, for several type I superconductors, where one sees that the experimental measurements fall into the line with a slope of $7/2$, i.e, 3.5 as predicted by the BCS theory. The band gap solution (normalized to its value at $T = 0$) as function of the temperature (normalized to T_c) for three different metals (Niobium, Tantalum and Tin) and the BCS theoretical solution are shown in Fig.2.2b, and one sees that the experimental results agree with the theoretical one. The decrease of the band gap energy as the temperature approaches its critical value can be interpreted as the weakening of the binding energy, in this case between electrons.

The band gap equation, Eq. 2.1, can be obtained by applying the mean field approach to the superconducting pairing Hamiltonian, and minimizing the respective free energy with respect to the superconducting gap [9, 37]. In the case of a superconductor where several bands participate in the formation of the superconducting state, n superconducting gaps have to be considered. Thus, in the next sections we introduce the Hamiltonian of a n-band superconductor used in our work (which includes, already, a Zeeman term) and derive an expression for the free energy and the n-band gap equations.

2.2.1 BCS Hamiltonian of n-band superconductors

In this work we use a simple weak-coupling description of n-band superconductors, adopting the Hamiltonian introduced by Sulh, Matthias and Walker [38] with an additional Zeeman splitting term:

$$\begin{aligned} H - \mu N - \sigma h N &= \sum_{k\sigma i} \xi_{k\sigma i} c^{\dagger}_{k\sigma i} c_{k\sigma i} \\ &- \sum_{kk'ij} V^{ij}_{kk'} c^{\dagger}_{k\uparrow j} c^{\dagger}_{-k\downarrow j} c_{k'\uparrow i} c_{-k'\downarrow i}, \end{aligned} \tag{2.5}$$

where i, j are the band index, μ is the chemical potential, $c^{\dagger}_{k\sigma i}[c_{k\sigma i}]$ creates (annihilates) a i-band electron with momentum k and spin $\sigma = \uparrow, \downarrow$ spin along the in-plane magnetic field, $h = \mu_B H$, where μ_B and H are, respectively, the Bohr magneton and the in-plane applied magnetic field,

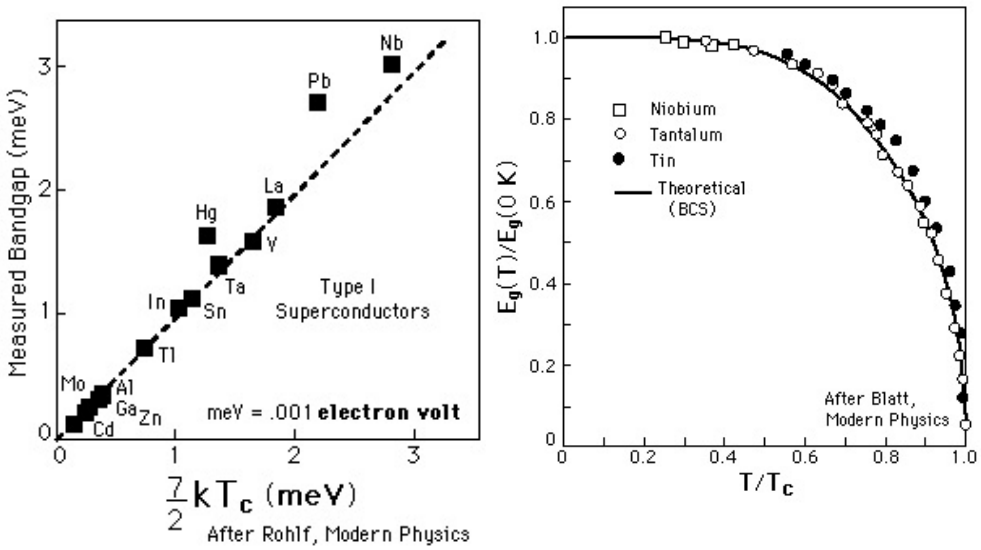

(a) (b)

Figure 2.2: (a) Experimental measurements of the band gap energy and respective critical temperature for several type I superconductors. The data is in agreement with the BCS prediction. (b) Superconducting gap (normalized to its value at zero temperature) as function of temperature (normalized to T_c) for Niobium, Tantalum and Tin and BCS theoretical prediction. The experimental data fall into the theoretical curve.

$\xi_{ki}^{\sigma} = \varepsilon_{ki} - \mu - \sigma h$ is the kinetic energy term measured from μ and $V_{\mathbf{kk}'}^{ij}$ gives the intraband ($i = j$), and interband ($i \neq j$) pairing interactions.

Having in mind the application of the mean field approach to the above Hamiltonian expression, we introduce the Bogoliubov-Valatin transformation

$$\begin{pmatrix} \gamma_{k\uparrow j}^{\dagger} \\ \gamma_{-k\downarrow j} \end{pmatrix} = \begin{pmatrix} u_{kj} & -v_{kj} \\ v_{kj} & u_{kj} \end{pmatrix} \begin{pmatrix} c_{k\uparrow j}^{\dagger} \\ c_{-k\downarrow j} \end{pmatrix},$$

with

$$\{\gamma_{k\uparrow i}^{\dagger}, \gamma_{k'\uparrow j}\} = \delta_{kk'}\delta_{ij}, \tag{2.6}$$

where γ and $\gamma^{\dagger}$ are the fermionic operators, u_k and v_k are real and obey to the condition $|u_k|^2 + |v_k|^2 = 1$. One also uses the expression for the thermal average of an operator

$$\langle \hat{O} \rangle = \frac{Tr(\hat{O}e^{-\beta H})}{Tr(e^{-\beta H})} \tag{2.7}$$

to calculate the thermal average of the kinetic term

$$\sum_{k\sigma i} \xi_{ki}^{\sigma} c_{k\sigma i}^{\dagger} c_{k\sigma i}, \tag{2.8}$$

which gives

$$\sum_{k\sigma i}\{v_{ki}^2\xi_{ki}^{\sigma}+[\xi_{ki}(u_{ki}^2-v_{ki}^2)]f(E_{ki}^{\sigma})\}, \tag{2.9}$$

where $f(E_{ki}^{\sigma})=\langle\gamma_{ki\sigma}^{\dagger}\gamma_{ki\sigma}\rangle$ is the ideal fermi gas occupation number and $E_{ki}^{\sigma}=E_{ki}+\sigma h$.

Using the mean-field approximation in this Hamiltonian one obtains a new expression for the Hamiltonian as the sum of a term H_0 for the independent quasi-particle excitations and a constant term C representing the thermal average of the Hamiltonian,

$$H=H_0+C, \tag{2.10}$$

with

$$H_0=\sum_{k\sigma i}E_{ki}^{\sigma}\gamma_{k\sigma i}^{\dagger}\gamma_{k\sigma i}, \tag{2.11}$$

$$E_{ki}^{\sigma}=\sqrt{\xi_{ki}^2+|\Delta_{ki}|^2}+\sigma h, \tag{2.12}$$

where E_{ki}^{σ} gives the excitation spectrum, and

$$\begin{aligned} C &= \sum_{k\sigma i}\{v_{ki}^2\xi_{ki}+[\xi_{ki}(u_{ki}^2-v_{ki}^2)-E_{ki}]f(E_{ki}^{\sigma})\} \\ &- \sum_{kk'i}V_{kk'}^{ii}u_{ki}v_{ki}u_{k'i}v_{k'i}(1-f(E_{ki}^{\uparrow})-f(E_{ki}^{\downarrow}))(1-f(E_{k'i}^{\uparrow})-f(E_{k'i}^{\downarrow})) \\ &- 2\sum_{k,k',j>i}V_{kk'}^{ij}u_{ki}v_{ki}u_{k'j}v_{k'j}(1-f(E_{ki}^{\uparrow})-f(E_{ki}^{\downarrow}))(1-f(E_{k'j}^{\uparrow})-f(E_{k'j}^{\downarrow})). \end{aligned} \tag{2.13}$$

2.2.2 Free energy

The free energy of a system can be calculated from the expression

$$\begin{aligned} F &= -k_BT\ln Z \\ &= -\frac{1}{\beta}\ln[Tr(e^{-\beta(H_0+C)})] \\ &= -\frac{1}{\beta}\sum_{k\sigma i}\ln(1+e^{-\beta E_{ki}^{\sigma}})+C \\ &= k_BT\sum_{k\sigma i}\ln(1-f(E_{ki}^{\sigma}))+C, \end{aligned} \tag{2.14}$$

where Z is the partition function and $\beta=1/k_BT$.

Using the conditions resulting from the minimization of the free energy with respect to v_{ki},

$$\Delta_i^2=E_{ki}^2-\xi_{ki}^2, \tag{2.15}$$

$$v_{ki}^2=\frac{1}{2}\left(1-\frac{\xi_{ki}}{E_{ki}}\right), \tag{2.16}$$

$$u_{ki}v_{ki} = \frac{\Delta_i}{2E_{ki}}, \tag{2.17}$$

$$u_{ki}^2 - v_{ki}^2 = \frac{\xi_{ki}}{E_{ki}}, \tag{2.18}$$

and defining the quantities

$$\Delta_i = \sum_j V_{ij}\delta_j \tag{2.19}$$

and

$$\delta_j = \sum_k u_{kj}v_{kj}(1 - f(E_{kj}^{\uparrow}) - f(E_{kj}^{\downarrow})), \tag{2.20}$$

one obtains

$$\delta_i - \sum_k \frac{\Delta_i}{2E_{ki}} = -\sum_k \frac{\Delta_i}{2E_{ki}}[f(E_{ki}^{\uparrow}) + f(E_{ki}^{\downarrow})], \tag{2.21}$$

and one ends up with

$$F_s = k_B T \sum_{k\sigma i} \ln[1 - f(\left|\xi_{ki}^{\sigma}\right|)] + \sum_{ki}(\xi_{ki} - E_{ki}) + \sum_i \delta_i\Delta_i. \tag{2.22}$$

The normal state free energy corresponds to the case $F_n = F_s(\Delta_i = 0)$, i.e., $E_{ki}^{\sigma} \to \left|\xi_{ki}^{\sigma}\right| = \left|\xi_{ki}\right| - \sigma h$, so that

$$F_n = k_B T \sum_{k\sigma i} \ln[1 - f(\left|\xi_{ki}^{\sigma}\right|)] + 2\sum_{|k|<k_F} \xi_{ki}, \tag{2.23}$$

where $\mu = \varepsilon_F$ is assumed. Finally the free energy difference between states is

$$\begin{aligned}
\Delta F &= F_s - F_n \\
&= k_B T \sum_{k\sigma i} \ln\left[\frac{1 - f(E_{ki}^{\sigma})}{1 - f(\xi_{ki}^{\sigma})}\right] + \sum_{ki}(\xi_{ki} - E_{ki}) - 2\sum_{|k|<k_F} \xi_{ki} + \sum_i \delta_i\Delta_i \\
&= k_B T \sum_{k\sigma i} \ln\left[\frac{1 - f(E_{ki}^{\sigma})}{1 - f(\xi_{ki}^{\sigma})}\right] + 2\sum_{|k|>k_F,i} (\xi_{ki} - E_{ki}) + \sum_i \delta_i\Delta_i.
\end{aligned} \tag{2.24}$$

The calculations of the free energy differences in our work were carried out using this equation in the continuum limit where the first two sums were turned into integrals limited by the Debye frequency ω_D, with the approximation $\frac{\hbar\omega_D}{\Delta_i} \gg 1$.

2.2.3 *n*-band gap equations

Minimizing the free energy difference with respect to the superconducting order parameters Δ_i, one obtains an expression for the coupled n-band superconducting gap equations, where s-wave symmetry is assumed,

$$\Delta_i = \sum_j V_{ij}\delta_j, \tag{2.25}$$

with

$$\begin{aligned} \delta_j &= \delta_j(T,h,\Delta_j,N_j(\xi)) && (2.26)\\ &= \int_0^{\omega_D} d\xi_j \Delta_j K_j(\xi_j,\Delta_j,T,h), && (2.27) \end{aligned}$$

where

$$K_j(\xi_j,\Delta_j,T,h) = \frac{N_j(\xi)}{2E_j(\xi,\Delta_j)}\left(\tanh\frac{E_j(\xi,\Delta_j)+h}{2k_BT}+\tanh\frac{E_j(\xi,\Delta_j)-h}{2k_BT}\right), \qquad (2.28)$$

where $E_j=\sqrt{\xi^2+\Delta_j^2}$ is the quasi-particle excitation energy of band j, ω_D is the usual frequency cutoff, and $N_j(\xi)$ is the DOS of band j.

Chapter 3

Zeeman splitting effects in one-, two- and n-band metallic superconductors

As stated in the Introduction, one of the objectives of our work is the study of critical magnetic fields in one- and two-band graphene based superconductors. In order to realize the role of the semi-metallic density of states of the graphene band, the understanding of the typical behaviour of the band gap solutions and phase diagrams of one- and a two-band metallic superconductors is required and such study is carried out in this chapter. For the purpose of studying the Zeeman splitting effects in these superconductors we use the n-band gap equations, Eq. 2.26, derived in the previous chapter, for $i, j = 1$ and $i, j = 1, 2$, respectively, and for $N_j(\xi) = 1$.

3.1 One-band gap solutions

Adapting Eq. 2.26 to the one-band case by doing $i, j = 1$, one obtains

$$\Delta_1 = V_{11} \int_0^{\omega_D} d\xi \Delta_1 \frac{N_1(\xi)}{2E_1(\xi,\Delta_1)} \left(\tanh \frac{E_1(\xi,\Delta_1)+h}{2k_BT} + \tanh \frac{E_1(\xi,\Delta_1)-h}{2k_BT} \right). \tag{3.1}$$

Since both Δ_1 and N_i do not depend on ξ (N_i can be, in the case of metallic bands, considered constant in ξ), one may put them outside of the integral and Eq. 3.1 becomes

$$\frac{1}{V_{11}N_1} = \int_0^{\omega_D} d\xi \frac{1}{2E_1(\xi,\Delta_1)} \left(\tanh \frac{E_1(\xi,\Delta_1)+h}{2k_BT} + \tanh \frac{E_1(\xi,\Delta_1)-h}{2k_BT} \right). \tag{3.2}$$

Eq. 3.2 provides a relation between Δ, T, h and V. From this equation one may ascertain if there is a superconducting critical temperature for any finite intraband interaction, thus respecting the BCS criterion for a material to be considered a superconductor. To determine, T_c one sets $\Delta_1 = 0$ and $h = 0$ in Eq. 3.2. The intraband interaction dependence of the critical temperature, T_c *vs.* V, is plotted in Fig. 3.1, where one sees that T_c is always finite even for arbitrary small intraband interactions. A finite critical magnetic field, h_c, should also be present for any finite intraband

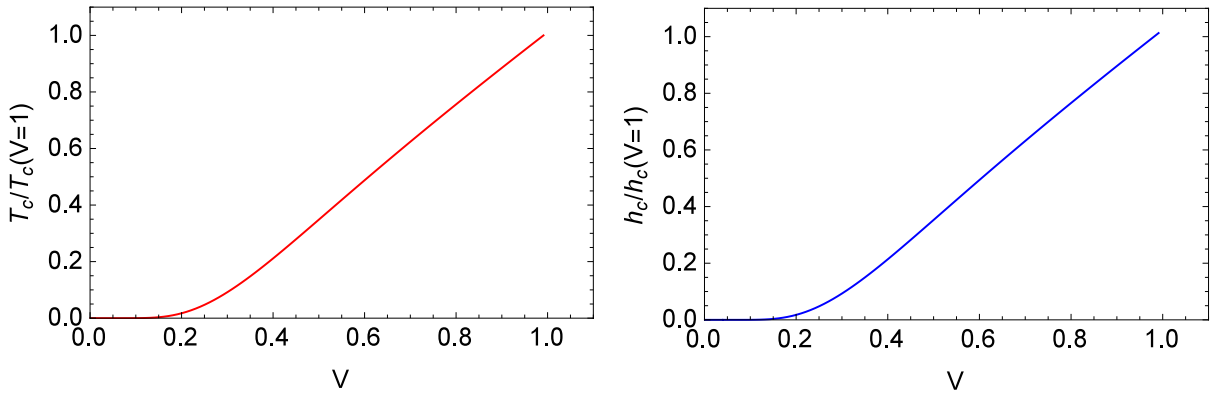

Figure 3.1: (a) Critical temperature and (b) critical magnetic field versus metallic intraband interaction. In both cases, a finite critical value is present for arbitrarily small intraband interactions.

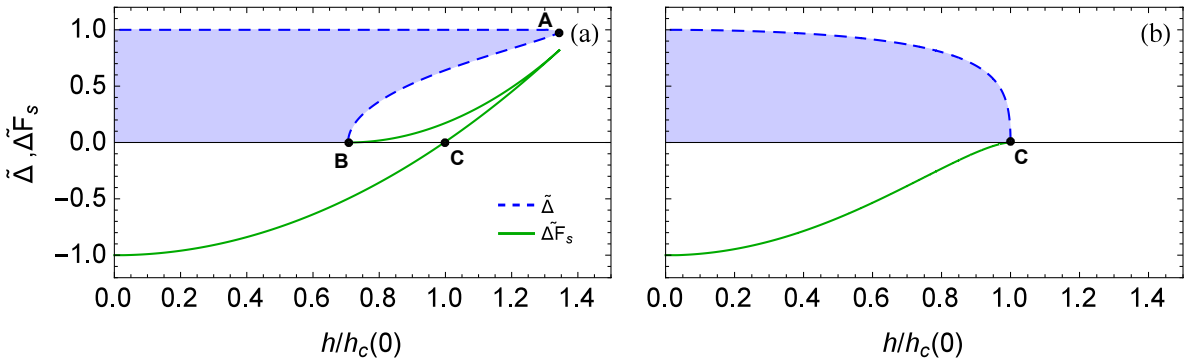

Figure 3.2: (a) $T = 0$ and (b) $T = 0.6T_c$ band gap and free energy difference solutions (normalized to the zero field value) versus in-plane magnetic field (normalized to the zero temperature critical field), for a one-band superconductor. In (a) a "jump" occurs in the band gap solution to $\Delta = 0$ at the critical field while in (b) the transition occurs smoothly, corresponding to first- and second-order transitions, respectively.

---

interaction. To determine h_c one sets $\Delta_1 = 0$ and $T = 0$ in Eq. 3.2. As one sees in Fig. 3.1, where the critical field *vs.* intraband interaction function is plotted, there is, also, a critical magnetic field for arbitrary small intraband interactions.

In order to study Zeeman splitting effects in superconducting systems, one studies the band gap solutions as functions of the magnetic field for different temperatures, using again Eq. 3.2. At the same time, the free energy difference solution is determined since changes in its sign correspond to phase transitions. Next, we discuss the band gap and free energy difference solutions for $T = 0$ and $T = 0.6T_c$, for $V_{11} = 1.0$.

The zero temperature band gap and free energy difference solutions are shown in Fig. 3.2 a). By definition, the phase transition between the normal and the superconducting state, which

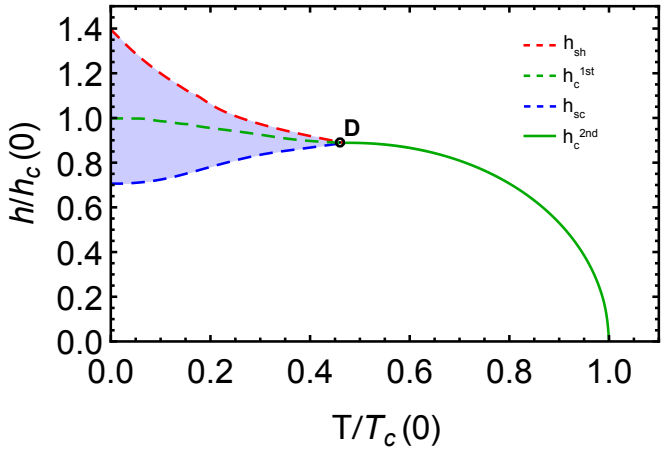

Figure 3.3: In-plane magnetic field (normalized to the zero temperature critical field) *vs.* temperature (normalized to the zero field critical temperature) phase diagram of a one-band superconductor. The low temperature first-order transition (dashed green curve) becomes one of second-order (solid green curve) at the tricritical point $T \approx 0.56T_c$ (point D).

occurs at the critical magnetic field, happens when the total free energy difference changes sign. Thus, one could expect that the value of the band gap parameter would decrease smoothly with increasing field till zero at h_c (in a similar way as Fig. 2.2b). However, for $T = 0$ [see Fig. 3.2 a)], the gap solution shows a reentrant behavior around h_c (point C) which is limited by the superheating field, h_{sh}, (maximum field with maximum band gap value, point A) and by the supercooling field, h_{sc} (minimum field with zero band gap, point B). This means that Δ_1 is finite at h_c (point C), and consequently, at the transition, a jump occurs, in the band gap solution, from a non-zero to a zero value. This type of transition, called first-order transition, happens when the free energy contains several local minima and the transition occurs without convergence of local extreme. When one increases the temperature up to values close to T_c [see Fig. 3.2 b)], the gap solution decreases continuously till zero, meaning that the transition is a second-order transition. In this case, the free energy absolute minimum converges to another local extreme with increasing magnetic field.

The low temperature reentrant behaviour of the band gap solution implies a metastability region in the in-plane magnetic field *vs.* temperature phase diagram of quasi-2D one-band superconductors (blue shaded area in Fig. 3.3), limited above by h_{sh} (dashed red curve) and below by h_{sc} (dashed blue curve) and a first-order transition (dashed green curve). This region extends up to a tricritical point $T^\star \approx 0.56T_c$ (point D) from which the first-order transition becomes a second-order transition.

3.2 Two- and n-band gap solutions

Adapting again Eq. 2.26, this time for the two-band case (by doing $i, j = 1, 2$) one obtains the two following coupled equations

$$\Delta_1 = V_{11}\int_0^{\omega_D} d\xi_1 K_1(\xi_1,\Delta_1,T)\Delta_1 + V_{12}\int_0^{\omega_D} d\xi_2 K_2(\xi_2,\Delta_2,T)\Delta_2, \tag{3.3}$$

and

$$\Delta_2 = V_{21}\int_0^{\omega_D} d\xi_1 K_1(\xi_1,\Delta_1,T)\Delta_1 + V_{22}\int_0^{\omega_D} d\xi_2 K_2(\xi_2,\Delta_2,T)\Delta_2. \tag{3.4}$$

Below we discus the cases $V_{12} = 0$ and $V_{12} \neq 0$.

3.2.1 $V_{12} = 0$

One immediately concludes that by doing $V_{12} = 0$ in Eqs. 3.3 and 3.4 one recovers the one-band gap equation. The $T = 0$ and $T = 0.6T_c$ band gap solutions (and the respective free energies) and the in-plane magnetic field *vs* temperature phase diagram, for $V_{11} = 1.0$, $V_{22} = 0.9$ and $V_{12} = 0$, are shown in Figs. 3.4 a), 3.5 a) and Fig. 3.6 a), respectively. In a two-band superconductor, with $V_{12} = 0$, there are two band gap solutions, two first/second-order transition curves at low/large temperatures [see Figs. 3.4 a) and 3.5 a)], and two metastability regions are present in the phase diagram [see Fig. 3.6 a)]. The curves with the largest Δ values in the band gap solutions [dashed blue lines in Figs. 3.4 a) and 3.5 a)], the first-order and second-order curves as well the metastability region [dashed green curve, solid green curve and blue shaded area in Fig. 3.6 a)] which lie at the phase diagram zone of largest fields and low temperatures, correspond to the band with the largest intraband interaction, i.e., V_{11} in this case. Even though two phase transition are present in the phase diagram, only one of these transitions corresponds to the superconducting-normal state transition. Indeed, the transition associated to the band with the smallest intraband interaction, V_{22}, lies within the superconducting region of the phase diagram. This transition can be interpreted as a transition between superconducting states. Thus, the transition associated to the band with the largest intraband interaction is the one that leads our system from a superconducting to a normal state.

3.2.2 $V_{12} \neq 0$

When the interband interaction is finite, the bands are no longer independent from each other. Indeed, for any finite interband interaction ($V_{12} \neq 0$) the value of Δ_1 not only depends on V_{11} and $N_1(0)$ but also on the interaction V_{12} and on the density of states (at the Fermi level) of the band 2 and vice versa [see Eqs. 3.3 and 3.4]. Therefore, instead of analysing separately the free energies of the two bands, the sum of them is analysed. In a n-band superconductor, the interband interaction leads, qualitatively, to a $-\Delta_i\Delta_j\cos(\phi_{ij})$ coupling term in the free energy, where ϕ_{ij} is the relative phase of Δ_i and Δ_j. The local extreme of the free energy have $\phi_{ij} = 0$ or $\phi_{ij} = \pi$, but all local minima have $\phi_{ij} = 0$ if the interactions are attractive. In our work we consider $\phi_{ij} = 0$, i.e., Δ_1 and Δ_2 are in phase, and consequently, V_{ij} generates a $-\Delta_i\Delta_j$ term in the free energy which leads to a positive shift of both band gaps and an increase in T_c (and h_c).

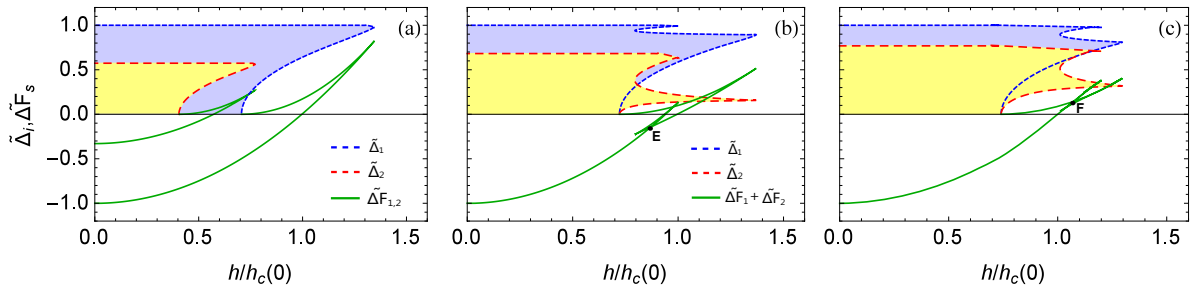

Figure 3.4: Zero temperature superconducting gap (normalized to the zero field value of the band 1) and free energy difference solutions (normalized to the zero field value) versus in-plane magnetic field (normalized to the zero temperature critical field), of a two-band metallic superconductor, for $V_{11} = 1.0$, $V_{22} = 0.9$ and for (a) $V_{12} = 0.0$, (b) $V_{12} = 0.04$ and (c) $V_{12} = 0.1$. In all three cases a jump occurs, on the band gap solution, at the critical field, to $\Delta = 0$, which correspond to first-order transitions. In (a), since there is no interband interaction, one recovers the zero temperature one-band gap solutions. In (b), a non-zero interband interaction forces Δ_1 to "follow" Δ_2 and vice-versa, and as result a second reentrance appears in the band gap solutions. In (c), due to a large enough interband interaction, the crossing in the free energy is shifted above zero, meaning that there is no phase transition between superconducting states.

This shift is larger for the band with smallest V and consequently smallest Δ, (in our case, the band 2) because Δ_i depends on the factor $\Delta_j V_{ij}$. Furthermore, the coupling of the bands implies also that if Δ_1 is nonzero at the local minima, then Δ_2 is also nonzero [if one does $\Delta_1 = 0$ in Eqs. 3.3 or 3.4 automatically $\Delta_2 = 0$].

These features can be observed in Figs. 3.4 b) and 3.5 b), where the band gap solutions were obtained for a finite (but much smaller than the intraband pairings V_{11} and V_{22}) interband interaction $V_{12} = 0.04$ for $T = 0$ and $T = 0.6T_c$, respectively. One also identifies not only one but two reentrances in the band gap functions, such that the extra reentrance of the band 1 is found at the region where the main reentrance of the band 2 appears, and vice-versa. This means that the interband interaction forces Δ_1 to "follow" Δ_2 and vice-versa. Furthermore, one also identifies a crossing in the total free energy solution [Fig. 3.4 b), solid green curve, point E), which represents an additional phase transition. This crossing occurs before the sign change of $F_s - F_n$ (where another phase transition occurs) reflecting a first-order transition within the superconducting phase followed by the first-order superconducting-normal phase transition. However, as one sees in the phase diagram in Fig. 3.6 b), the large temperature second-order transition between superconducting states disappears.

As one increases V_{12}, but still in the weak coupling regime, the crossing in the free energy, at low temperature, is shifted above the $F_s - F_n = 0$ level [see Fig. 3.4 c), solid green curve, point F] and the first-order transition between superconducting states converges towards the first-order transition from the superconducting to the normal state and disappears as it crosses this curve [see the phase diagram plotted at Fig. 3.6 c)]. Therefore no transition within the superconducting phase occurs. For temperatures close to T_c, Figs. 3.5 b) and 3.5 c), it can be, again, identified a second-order transition where both gaps go to zero. From the case of Fig. 3.5 b) to Fig. 3.5

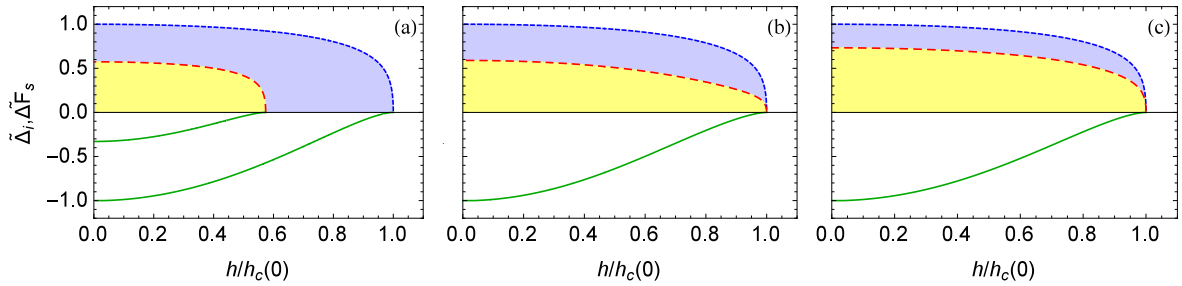

Figure 3.5: Superconducting gap (normalized to the zero field value of the band 1) and free energy difference solutions (normalized to the zero field value) versus in-plane magnetic field (normalized to the zero temperature critical field), of a two-band metallic superconductor, at $T = 0.6T_c$, for $V_{11} = 1.0$, $V_{22} = 0.9$ and for (a) $V_{12} = 0.0$, (b) $V_{12} = 0.04$, (c) $V_{12} = 0.1$. In all three cases the superconducting gap decrease, with increasing field, smoothly till zero, where a second-order transition occurs. In (a), since there is no interband interaction, one recovers again the zero temperature one-band gap solutions and thus, there is one second-order transition associated to each band (two in total). In (b) and (c), due to non-zero interband interactions, in total, only one second-order transition occurs.

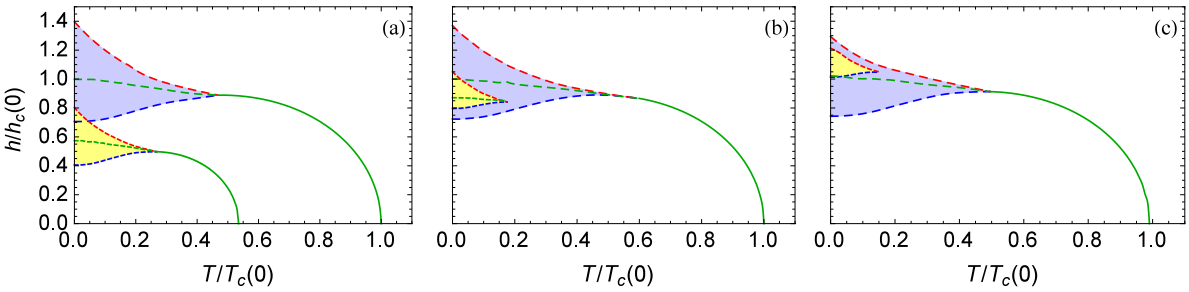

Figure 3.6: In-plane magnetic field (normalized to the zero temperature critical field) *vs* temperature (normalize to the zero field critical temperature) phase diagram, of a two-band metallic superconductor, for $V_{11} = 1.0$, $V_{22} = 0.9$ and for (a) $V_{12} = 0.0$, (b) $V_{12} = 0.04$, (c) $V_{12} = 0.1$. One can confirm the features pointed out in Figs. 3.4 and 3.5: (a) two metastability regions, two first-order and second order-transitions; (b) the second-order transition associated to the band with smallest gap values (band 2) disappears; (c) the first-order transition associated to the band 2 disappears as it crosses the first-order transition associated to the band 1.

---

c) [as well from Fig. 3.4 b) to Fig. 3.4 c)] an increase of the band gap values occurs due to the increase of the interband interaction.

Some of the changes from the $V_{12} = 0$ to the $V_{12} \neq 0$ cases are more or less expected but why does the second order transition of the band 2 disappear? Indeed this question can be answered. Considering $(t_{c2}^{\circ}, h_{c2}^{p})$ the second-order transition point of the band 2 for the uncoupled case, the free energy in the neighborhood of the critical point is qualitatively of the form

$$F_s - F_n \approx \Delta F_1^{\circ}(\Delta_1, t, h) + a_2(t,h)\Delta_2^2 + b_2\Delta_2^4 - \alpha\Delta_1\Delta_2, \tag{3.5}$$

where α is a small constant proportional to the interband coupling, ΔF_1° is the free energy dif-

ference associated with band 1 in the uncoupled case, a_2 vanishes as $(t,h) \to (t_{c2}^{\circ}, h_{c2}^{p})$ and Δ_1, Δ_2 are absolute values. The local extreme is obtained from the conditions $\partial F_s/\partial \Delta_1 = 0$, $\partial F_s/\partial \Delta_2 = 0$ and solving them we get a new condition, $\Delta_1 \approx \Delta_1^{\circ}$ (since Δ_2 is small in the neighborhood of the transition point) that leads to $2a_2(t,h)\Delta_2 + 4b_2\Delta_2^3 - \alpha\Delta_1 = 0$. The term $-\alpha\Delta_1$ can be considered constant around $(t_{c2}^{\circ}, h_{c2}^{p})$ and therefore, as α is turned on, the solution $\Delta_2^{\circ} = 0$ is shifted to negative values and becomes irrelevant. Only the finite gap solution for Δ_2 remains. This solution approaches zero only when Δ_1 goes to zero, that is, near the transition point $(t_{c1}^{\circ}, h_{c1}^{p})$. When $(\Delta_1, \Delta_2) \to (0,0)$, there is a second-order phase transition, since the point $(\Delta_1, \Delta_2) = (0,0)$ is a local extreme of the free energy and a second-order transition results from the convergence of two local extreme, one of them being the absolute minimum.

3.2.3 $V_{ij} \approx V_{ii}$ case

Although we have studied the effect of a interband interaction on a two-band conductor system, the value used for the interband interaction was much smaller than the intraband interaction. If the band gaps "follow" each other when under a weak interband interaction, what can happen for a strong one? Indeed, increasing the interband interaction to a sufficient strong one can lead a two-band superconductor to behave as a typical one-band superconductor.

The $V_{ij} \approx V_{ii}$ case can be simplified, for a two-band case, in two different ways. One may consider a V_{ij} of the order of V_{ii}, i.e., $V_{12}^2 = V_{11}V_{22}$. Using this condition and the two coupled gap equations, one has $\Delta_2 = \sqrt{V_{11}/V_{22}}\Delta_1$ and a small region of enhanced fluctuations remains in this case. In an more extreme example, when V_{ij} is much stronger than V_{ii}, $V_{12} \gg V_{11}$ and $V_{12} \gg V_{22}$, one has $\Delta_2 \approx \Delta_1$ and that is not more than the one-band case.

3.2.4 n-band case

The features observed in this chapter, in particular the ones for a two-band metallic superconductor, can be generalized to (quasi-2D) n-band superconductors. The transition between the superconducting and the normal state is associated to the band with the largest band gap values and additional low temperature FOT curves (more precisely, $n-1$ curves) and the corresponding metastability regions appear within the superconducting region of the phase diagram, each characterized by a large reduction in the superconducting gap of the band directly associated with the transition [37, 39].

Chapter 4

Zeeman splitting effects in undoped and doped isolated graphene

In this chapter, we discuss the mean-field superconducting phase diagram of a single graphene sheet under parallel magnetic field. We start by describing the graphene electronic band structure, more concretely, we calculate the energy band dispersion and the density of states, the latter being needed to solve the band gap equation, Eq. 2.26. Next, we find if a superconducting phase is present in a graphene band, given different values of pairing strength, V, and doping, μ, at zero magnetic field. Finally, a study on metastability regions in the in-plane magnetic field versus temperature phase diagram of superconducting graphene is addressed for different values of doping.

4.1 Energy band dispersion and density of states

The graphene electronic structure is composed by σ-bonds and π-bonds which give rise to, respectively, σ-bands and π-bands. The σ-bands have a filled shell forming deep valence bands [40]. Since each p-orbital has one extra electron, the π-bands are half filled making these bands important for electronic properties [40]. Indeed, since all valence electrons (which are relevant for the solid state properties) are π-electrons, we are only interested in π-bands [41].

In order to calculate the band dispersion of graphene, one usually uses the tight-binding method to obtain the Hamiltonian of the system, H. This method consists in using an approximate set of wave functions based upon superposition of wave functions for isolated atoms located at each atomic site, R_i [42]. This model describes the properties of tightly bound electrons in solids. The electrons in this model should be tightly bound to the atom to which they belong and they should have limited interaction with the surrounding atoms [42]. As a result, in the proximity of each atom the wave function of the electron will be rather similar to the atomic orbital of the free atom it belongs to [42].

In the tight-binding Hamiltonian model one usually imposes the condition that electrons are only allowed to hop both to the nearest and the next-nearest neighbor atoms of the lattice [40].

It can be written as

$$\begin{aligned} H = & -t_1 \sum_{\langle i,j\rangle,\sigma} (a^{\dagger}_{i,\sigma} b_{j,\sigma} + h.c.) \\ & - t_2 \sum_{\langle\langle i,j\rangle\rangle,\sigma} (a^{\dagger}_{i,\sigma} a_{j,\sigma} + b^{\dagger}_{i,\sigma} b_{j,\sigma} + h.c.), \end{aligned} \tag{4.1}$$

where $a_{\sigma i}$ ($a^{\dagger}_{\sigma i}$) annihilates (creates) an electron with spin σ ($\sigma = \uparrow, \downarrow$) on site R_i on sub-lattice A (equivalent definition for sub-lattice B), t_1 is the nearest neighbor hopping energy (hopping between different sub-lattices), t_2 is the next nearest neighbor hoping energy (hopping in the same sub-lattice).

The reason why the graphene lattice is divided into two sub-lattices, is that the graphene honeycomb lattice structure is not a Bravais lattice (because two neighboring sites are not equivalent [43]). Thus, the two-dimensional honeycomb lattice made out of hexagons is divided into two (A and B) interpenetrating triangular Bravais lattices with a two-atom basis [shown in Fig. 4.1a (left), reproduced from [40]] [43].

The nearest and the second nearest neighbors vectors of the hexagonal structure used in this model can be written as function of the sub-lattice vectors. The sub-lattice vectors $\vec{a}_1$ and $\vec{a}_2$ (real space unit vectors) can be written, in the (x,y) coordinates, as

$$\vec{a}_1 = \frac{a}{2}(3, \sqrt{3}), \vec{a}_2 = \frac{a}{2}(3, -\sqrt{3}), \tag{4.2}$$

and the three nearest and the six second-nearest neighbors vectors as

$$\vec{\delta}_1 = \frac{a}{2}(1, \sqrt{3}), \vec{\delta}_2 = \frac{a}{2}(1, -\sqrt{3}), \vec{\delta}_3 = -a(1,0), \tag{4.3}$$

$$\vec{\delta}'_1 = \pm a_1, \vec{\delta}'_2 = \pm a_2, \vec{\delta}'_3 = \pm(a_2 - a_1), \tag{4.4}$$

where $a \approx 0.142$ nanometers is the carbon-carbon distance.

In order to simplify the calculation of the energy band dispersion, the real space sub-lattice vectors are converted to the reciprocal space ($\vec{k}$-space). Consequently, and correspondingly, the reciprocal vectors ($\vec{k}$-space unit vectors) can be written as

$$\vec{b}_1 = \frac{2\pi}{3a}(1, \sqrt{3}), \vec{b}_2 = \frac{2\pi}{3a}(1, -\sqrt{3}). \tag{4.5}$$

Making a Fourier transformation one obtains the Hamiltonian in $\vec{k}$-space, which is given by

$$H = \sum_{\vec{k},\sigma} \Big(T_1 a^{\dagger}_{\vec{k},\sigma} b_{\vec{k},\sigma} + T_2 b^{\dagger}_{\vec{k},\sigma} a_{\vec{k},\sigma} + T_3 (a^{\dagger}_{\vec{k},\sigma} a_{\vec{k},\sigma} + b^{\dagger}_{\vec{k},\sigma} b_{\vec{k},\sigma}) \Big), \tag{4.6}$$

where the T_1, T_2 and T_3 coefficients are

$$\begin{aligned} T_1 &= -t_1 (2e^{i\frac{a}{2}k_x} \cos(\tfrac{\sqrt{3}}{2} a k_y) + e^{-iak_x}), \\ T_2 &= -t_1 (2e^{-i\frac{a}{2}k_x} \cos(\tfrac{\sqrt{3}}{2} a k_y) + e^{iak_x}), \\ T_3 &= -t_2 (4\cos(\tfrac{3}{2} a k_x) \cos(\tfrac{\sqrt{3}}{2} a k_y) + 2\cos(\sqrt{3} a k_y)). \end{aligned} \tag{4.7}$$

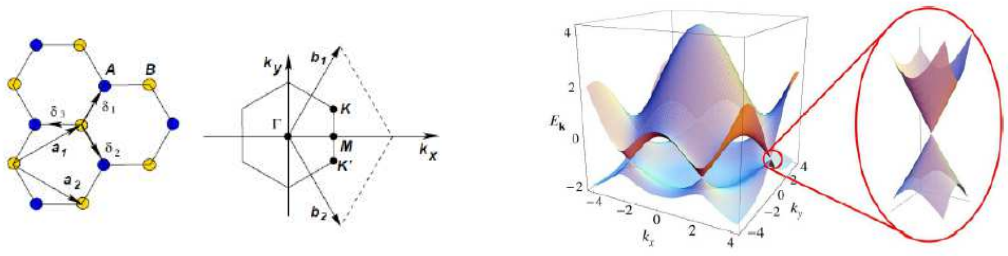

(a) (b)

Figure 4.1: (a) Graphene honeycomb lattice and its Brillouin zone. Left: lattice structure of graphene, made out of two interpenetrating triangular sub-lattices ($\vec{a}_1$ and $\vec{a}_2$ are the lattice unit vectors, and δ_1, δ_2, δ_3 are the nearest neighbor vectors). Right: corresponding Brillouin zone. High symmetry points K and K'. (b) Left: energy dispersion of a graphene band for $t_1 = 2.7eV$ and $t_2 = 0.2t_1$. Right: zoom in the energy dispersion at one of the Dirac points.

This Hamiltonian can be represented by a 2×2 matrix and the diagonalization of this matrix gives the band energy dispersion, as

$$E_{\pm}(\vec{k}) = \pm t_1 \sqrt{3 + f(\vec{k})} - t_2 f(\vec{k}), \tag{4.8}$$

with

$$f(\vec{k}) = 2\cos(\sqrt{3}ak_y) + 4\cos\left(\frac{\sqrt{3}}{2}ak_y\right)\cos\left(\frac{3}{2}ak_x\right), \tag{4.9}$$

where signs $+$ and $-$ correspond, respectively, to the upper (π) and lower (π^*) band. Around zero energy, π and π^* bands are symmetric for $t_2 = 0$ and are asymmetric for finite t_2.

$E(\vec{k})$ is a periodic function in the reciprocal lattice, and can be described within the first Brillouin zone [41] wherein are located the high symmetry points Γ, M, K and K' [shown in Fig. 4.1a (right), reproduced from [40]]. The latter two, usually called Dirac points [40]

$$\vec{K} = \left(\frac{2\pi}{3a}, \frac{2\pi}{3\sqrt{(}3)a}\right), \vec{K'} = \left(\frac{2\pi}{3a}, -\frac{2\pi}{3\sqrt{(}3)a}\right), \tag{4.10}$$

are of particular importance, and are localized at the corners of the graphene Brillouin zone. The energy dispersion is shown, for $t_1 = 2.7eV$ and $t_2 = 0.2t_1$, in Fig. 4.1b (reproduced from [40]). The Dirac cone [zoomed figure of Fig. 4.1b] is obtained by doing a expansion of Eq. 4.8 around the $\vec{K}$ point (as $\vec{k} = \vec{K} + \vec{q}$ with $|\vec{q}| \ll \vec{K}$), where $\vec{q}$ is the momentum measured relatively to the Dirac point $\vec{K}$, for finite t_1 and t_2,

$$\begin{aligned} E_{\pm}(\vec{k}) &\approx \pm t_1 \sqrt{(\tfrac{3a}{2}q_x)^2 + (\tfrac{3a}{2}q_x)^2 + O(q_x^3) + O(q_y^3)} \\ &= \pm v_F |\vec{q}| + O|q^2|, \end{aligned} \tag{4.11}$$

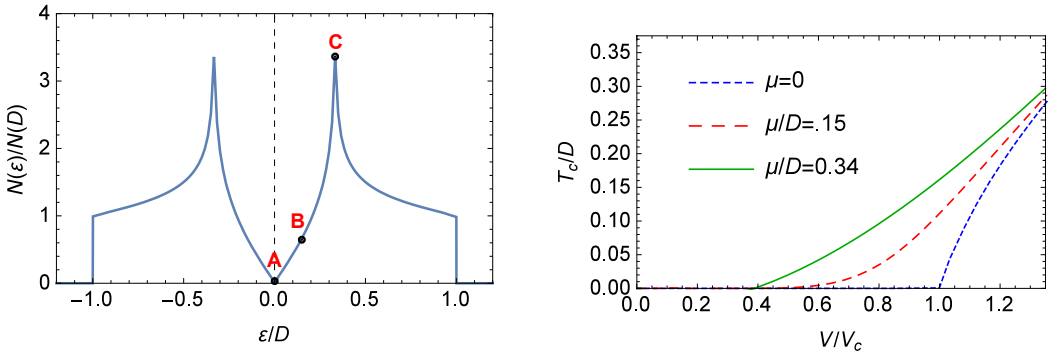

(a) (b)

Figure 4.2: (a) DOS of graphene (normalized to its value at the half-bandwidth D) as a function of energy (normalized to D). (b) Critical temperature at zero magnetic field (normalized to D) as a function of the BCS pairing interaction (normalized to the critical interaction value, V_c), for several values of doping, indicated by points A, B, and C in the top plot.

where $v_F = \frac{3}{2}t_1 a$ is the Fermi velocity.

The density of states of graphene, $N(\xi)$, can be obtained from the energy dispersion (Eq. 4.8). To simplify, we going consider $t_2 = 0$ and $t_1 = 1$ and the lattice constant equal to 1. The graphene density of states (normalized to its value at the half-bandwidth D) is shown in Fig. 4.2a. At low energy we can observe a linear behaviour. The points where the density of states diverges are called van-Hove singularities and these contribute more to the superconducting behavior, the closer to the Fermi level they are.

4.2 Critical intraband interaction

In the case of a single graphene band, we can determine from Eq.2.26 if a superconducting phase will be present given different values of pairing strength V and doping μ. If there is a superconducting phase, one should find a positive finite T_c when Δ is set to zero. The results for three different electron doping levels, $\mu/D = 0$, $\mu/D = 0.15$, and $\mu/D = 0.34$, are shown in Fig. 4.2b (the results are the same if we choose to hole dope the graphene band). In undoped graphene, there is a critical value of the pairing strength, which we call V_c, above which the system is a superconductor [44, 5]. As soon as we start doping, this critical interaction goes to zero, that is, for arbitrarily small V, T_c is *non-zero* (but very small). For a fixed V, T_c increases with μ up to the van Hove singularity energy [point C in Fig. 4.2a], reflecting the BCS dependence of T_c on the DOS around the Fermi energy. The curves in Fig. 4.2b share the same asymptotic behavior for $T_c \sim \Delta \gg \mu$.

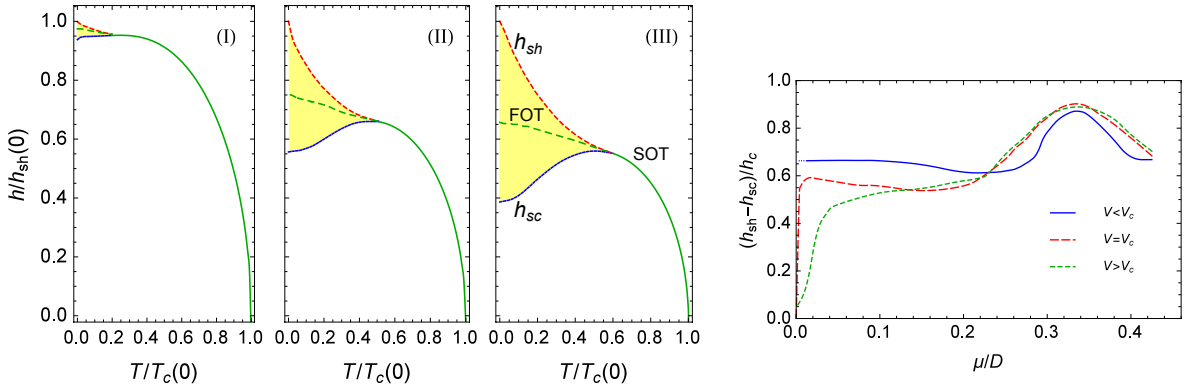

(a) (b)

Figure 4.3: (a) In-plane magnetic field (normalized to the zero temperature superheating field, $h_{sh}(0)$) vs. temperature (normalized to the zero field critical temperature, $T_c(0)$) phase diagram of graphene, for (I) $\mu/D = 0$, (II) $\mu/D = 0.15$, and (III) $\mu/D = 0.34$, for V =1.03 V_c. For $\mu = 0$, the metastability region (yellow shaded area) is very narrow and with doping, from (I) to (III), its normalized width increases as the Fermi energy is shifted away from the Dirac point. (b) Zero temperature width (normalized to the zero temperature critical field) behavior of the metastability region with doping, for $V = 0.78V_c$, $V = V_c$, $V = 1.03V_c$. The width is zero at $\mu = 0$ for $V = V_c$, but increases sharply for small μ. For $V = 0.78V_c$, low μ implies very small critical fields and temperatures, these values being out of the numerical range of our study and consequently not shown in the figure.

4.3 In-plane magnetic field *vs*. temperature phase diagram

The distinct DOS profile of graphene shown in Fig. 4.2a, and in particular its semi-metallic nature, is responsible for new features in the superconducting phase when an in-plane magnetic field is applied. The in-plane magnetic field *vs*. temperature superconducting phase diagram of a single graphene sheet for $V = 1.03V_c$, where $V_c/D = 0.0058$, and several values of chemical potential, $\mu/D = 0$, $\mu/D = 0.15$, and $\mu/D = 0.34$ (points A, B and C in Fig. 4.2a, respectively) is shown in Fig. 4.3a. The general behavior of the phase diagram, for the three cases, follows closely the one described in the Introduction for typical one-band superconductors, namely having a FOT curve between superconducting and normal phase at low temperatures, with its associated metastability region and becoming a SOT curve above some tricritical temperature, in the high temperature region of the phase diagram [29, 30]. There are, however, two important differences: the area of the normalized metastability region is not constant, as in typical weak coupling one-band metallic superconductors [30]. This area becomes very small (it vanishes as V goes, from above, to the critical interaction V_c) as doping goes to zero (that is, as the Fermi level approaches the Dirac point). Furthermore there is not a universal value for the tricritical temperature, which can take values $T^\star < 0.56T_{c0}$, becoming smaller as $\mu \to 0$ [see Fig. 4.3a (I)]. In the undoped case of Fig. 4.3a (I), the region of metastability is very narrow and becomes much larger for the intermediate doping level, at Fig. 4.3a (II), achieving its maximum width when the doping is such that the Fermi energy coincides with the van Hove singularity, as in Fig. 4.3a (III), as predicted in [31].

4.4 Metastability region width dependence with doping

The evolution of the zero temperature width of the metastability region with doping becomes more clear in Fig. 4.3b, where it is shown for three values of the pairing strength: $V = 0.78V_c$, $V = V_c$ and $V = 1.03V_c$. For the latter two cases, the zero temperature width of the metastability region increases sharply at low doping, nearly saturates at intermediate dopings, reaching its maximum value, when the doping factor shifts the Fermi level to the van Hove singularity, as can be seen in Fig. 4.3b. For $V = V_c$ the width is zero for $\mu = 0$. In contrast, for $V = 1.03V_c$ the width is finite everywhere, even when $\mu = 0$. In the first case, i.e., for $V = 0.78V_c$ the metastability region curve has a similiar behavior to the other two cases, however in this case the low μ behavior implies very low critical fields, outside the numerical range of our study.

Chapter 5

In-plane magnetic critical fields in undoped and doped GICs

In this chapter we present a study on the in-plane magnetic fields in undoped and doped GICs. We discuss the graphene-like band intraband interaction dependence in the in-plane field *vs*. temperature phase diagram and in the zero temperature band gap solutions. We also address a study on the doping dependence in the zero temperature band gap solutions, in particular we discuss the effect of doping in the, zero temperature, width of the metastability region.

5.1 Two-band description of GICs

As we mentioned in the Introduction, superconductivity was found in GICs several decades ago [12]. Since these compounds have a graphene-like band in the band structure, it is natural to ask how much of the behavior discussed in the previous chapter can be observed in these compounds. A simple approach one can use to address superconductivity in highly anisotropic GICs, while still preserving the essential characteristics of real materials, is a two-band model where one of the bands is treated as a graphene-like band and the other as a generic 2D metallic band. Highly anisotropic GICs are primarily stage-2 which, by definition, are composed of intercalated graphene bilayers. The DOS profile of graphene bilayers is different from that of a single graphene sheet of Fig. 4.2a [45], due to the splitting of the van Hove singularity and to a slight modification around the Fermi energy. Assuming that the energy scale of these features is much smaller than the GIC superconducting gaps, these differences can be neglected, i.e., one can assume the DOS shown in Fig. 4.2a even in the case of stage-2 GICs.

In what follows the metallic interlayer and graphene-like bands are labeled bands 1 and 2, respectively. The values considered for the matrix of potentials, necessary to find the superconducting gaps *via* Eqs. 3.3 and 3.4, are

$$\begin{pmatrix} V_{11} & V_{12} \\ V_{21} & V_{22} \end{pmatrix} N_1(0) \rightarrow \begin{pmatrix} 0.2 & 0.008 \\ 0.008 & V_{22} \end{pmatrix}, \tag{5.1}$$

where V_{11} is the intraband potential of the metallic interlayer band, V_{22} is the intraband potential

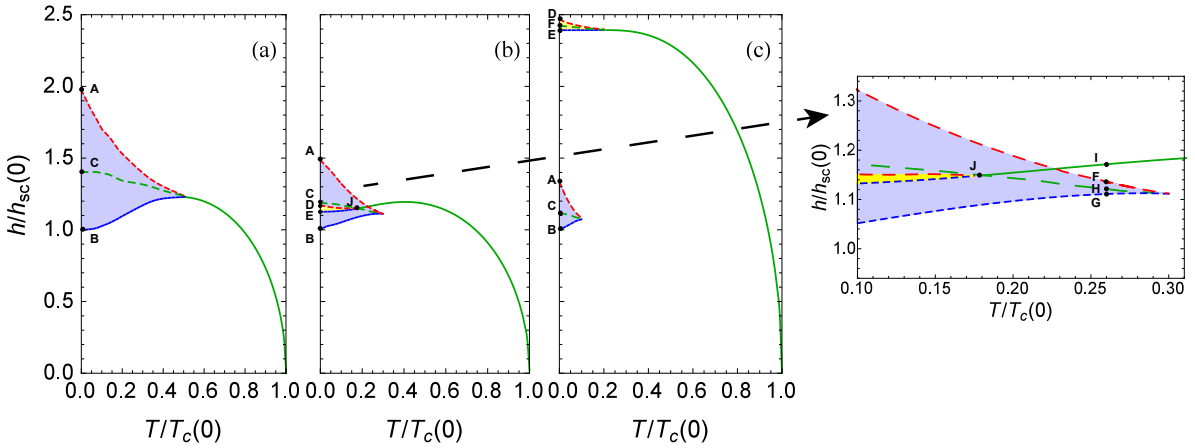

Figure 5.1: In-plane magnetic field (normalized to the zero temperature supercooling field, $h_{sc}(0)$) *vs*. temperature (normalized to the zero field critical temperature, $T_c(0)$) phase diagram of intercalated graphite (using a two-band BCS description) for (a) $V_{22} = 0.18$, (b) $V_{22} = 0.24$ and (c) $V_{22} = 0.26$. The metastability region associated primarily with intraband pairing in the metallic (graphene-like) band is shown in the blue (yellow) shaded area. From (a) to (c) the phase diagram changes from one of a typical one-band to one of a typical two-band superconductor phase diagram. In the intermediate case, (b), unusual behavior occurs: at the zoomed plot of (b) one sees, at a temperature $T \approx 0.175 T_c$, that the FOT (dashed green curve C-J) splits into a upper SOT (solid green curve J-I) and an additional lower FOT (dashed green curve J-H). The labeled points correspond to those in Figs. 5.2 and 5.3.

of the graphene-like band, $V_{12} = V_{21}$ is the interband potential which couples the two bands, and $N_1(0)$ is the density of states of the metallic band at the Fermi energy. The relation between the density of states of the graphene-like band and the metallic interlayer band is set by the condition $N_2(D) = 1.24 N_1(0)$, where $N_2(D)$ is the density of states of the graphene-like band at the band edge. To simplify the notation we will drop the $N_1(0)$ term when indicating interaction values.

5.2 In-plane field *vs*. temperature phase diagram and $T = 0$ band gap solutions

The existence of a finite interband coupling implies that the graphene-like band becomes superconducting (has a finite superconducting gap) for any value of V_{22}, even when the Fermi energy coincides with the Dirac point energy of the graphene-like band. Thus, there is not a critical value of the graphene-like intraband coupling as in the case of the isolated one-band graphene superconductor. This reflects the Josephson tunneling of Cooper pairs from the metallic band (this is similar to the effect of an external magnetic field in a paramagnetic system) and it is also the justification for the existence of a single critical superconducting temperature in the case a two-band superconductor with two metallic bands. However, a new critical intraband coupling V_{c2} for the graphene-like band can be defined, associated with the appearance of a second metastability region in the superconducting phase of the in-plane magnetic field *vs*. tem-

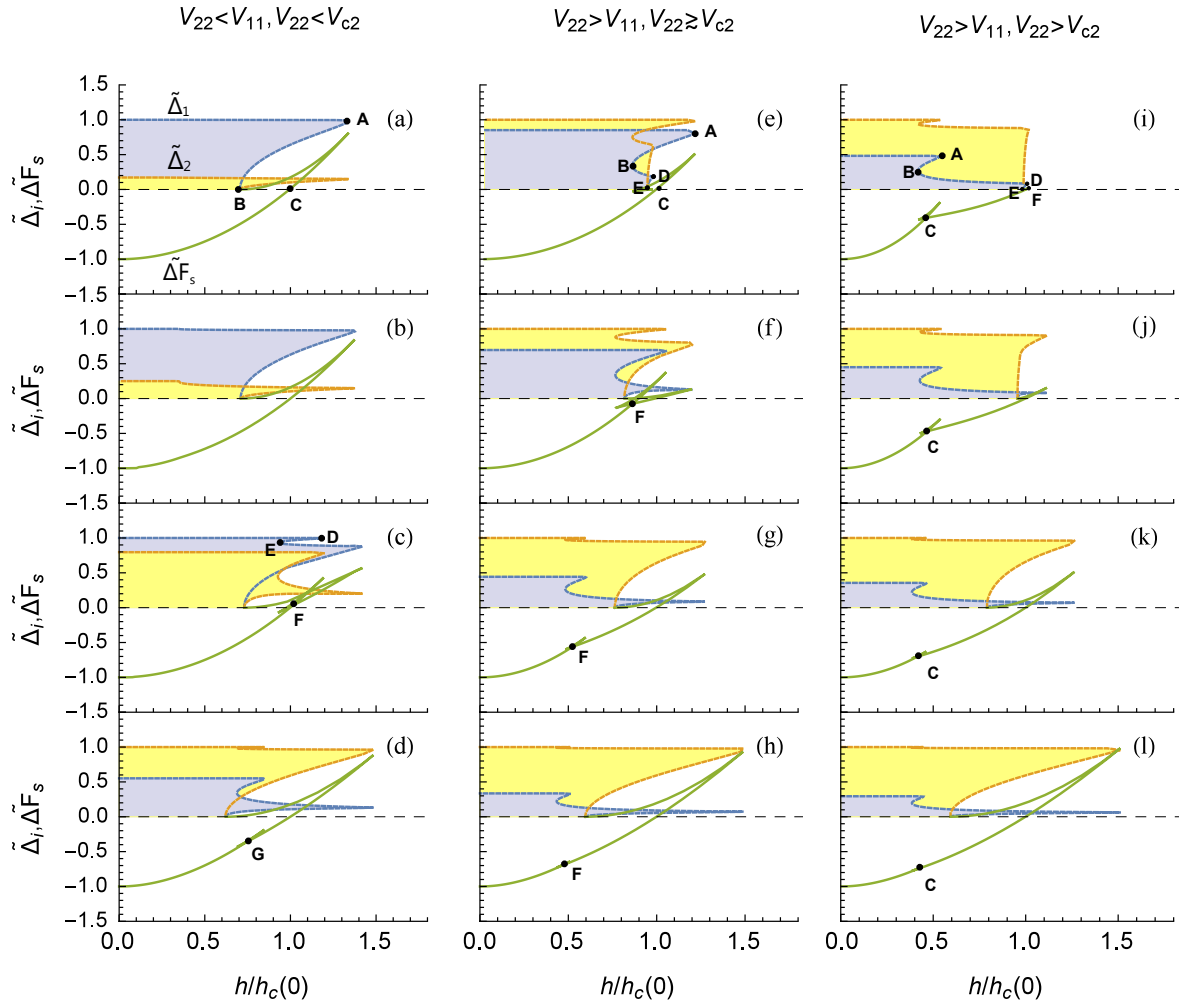

Figure 5.2: Zero temperature solutions of the coupled gap equations (normalized to the maximum gap) and the total free energy difference between the superconducting and the normal phases (normalized to its zero field value) of intercalated graphite. The in-plane magnetic fields are normalized to the zero temperature critical field, $h_c(0)$. The first, second and third columns correspond to $V_{22} = 0.18$, (a)-(d), $V_{22} = 0.24$, (e)-(h), and $V_{22} = 0.26$ (i)-(l), respectively and the first to the fourth rows correspond to $\mu = 0$, $\mu/D = 0.05$, $\mu/D = 0.15$, and $\mu/D = 0.34$, respectively. For $V_{22} = 0.18$, with increasing doping, the phase diagram changes from that of a typical one-band [(a)] to that of a two-band superconductor [(d)], as an additional reentrance (curve D-E) and FOT (point G) appear in the superconducting phase diagram. In (e), even though one identifies two reentrances, an additional FOT between superconducting phases only appears when we dope the graphene-like band (point F). In (i), the phase diagram shows typical two-band superconductor behavior.

perature phase diagram. This fact can be understood by the fact that the second metastability region reflects the existence of intrinsic pairing in the graphene-like band and this requires a finite intraband interaction. This second metastability region is always present in a two-band

superconductor when both bands have constant DOS at the Fermi energy and the interband coupling is weak. In the case studied here, for small V_{22}, the second metastability region is not present reflecting precisely the absence of intrinsic superconductivity in an isolated (weak coupled) graphene layer, in the weak interband coupling limit. Since V_{c2} depends on V_{11}, V_{22} and V_{12}, we do not normalize these interactions to a critical interaction, instead we choose to normalize the interactions to $N_1(0)$ as stated above.

5.2.1 Dependence on the intraband pairing of the graphene-like band

As before, by changing the doping factor μ, we are shifting the Fermi level in the graphene band, therefore changing the profile of $N_2(\xi)$ in Eqs. 3.3 and 3.4, whereas in the case of the metallic band, as usual in BCS theory, we consider a constant DOS, $N_1(\xi) = N_1(0)$. Firstly, we study our 2D model for $\mu/D = 0$, that is, the Fermi level coincides with the Dirac point energy of the graphene-like band DOS, for three different cases: $V_{22} = 0.18$, $V_{22} = 0.24$ and $V_{22} = 0.26$, these values being, respectively, smaller, slightly larger and larger than V_{c2}, where $V_{c2}/D = 0.006$. The in-plane magnetic field *vs*. temperature phase diagram for these three cases is shown in Fig. 5.1, and the corresponding zero temperature gap solutions and the total free energy difference between superconducting and normal phase as functions of the magnetic field is shown in Figs. 5.2(a), (e) and (i), respectively.

In the case of $V_{22} = 0.18$, the phase diagram obtained, Fig. 5.1(a), has the same behavior as that of a single-band BCS superconductor (only one metastability zone, blue shaded area, and one FOT, green curve which starts at the point C, are present in the phase diagram). This behavior can be confirmed from the zero temperature band gap solutions shown in Fig. 5.2(a) where one may observe, for each band, the presence of only one reentrance in the band gap solutions and no crossing in the free energy difference between superconducting and normal phase. This result implies that $V_{22} < V_{c2}$. Even though the graphene-like band is also superconducting (because Δ_2 is finite), since Δ_2 is much smaller than Δ_1, we may say that the superconductor behavior of this system is due to intrinsic superconducting correlations of the metallic interlayer band.

When one increases the graphene-like band intraband interaction to a value a little higher than V_{c2} (i.e., the case of $V_{22} = 0.24$), the influence of the graphene-like band is no longer negligible and even though there is no additional low temperature transition between superconducting phases, an extra metastability region, associated to the graphene-like band, appears (small yellow shaded region delimited by the point D, E and J in the Fig. 5.1). This behavior can be checked in Fig. 5.2(e), where one observes that there is no crossing in the free energy, but one observes the presence of two reentrances (points A-B and D-E) in the zero temperature band gap solutions. Since an additional FOT should be present in the phase diagram in order for it to be considered one of a typical two-band superconductor, for $V_{22} \gtrsim V_{c2}$ the system can be seen as an intermediate case between a one-band and a two-band superconductor. Furthermore, for temperatures in the $0.175T_c < T < 0.3T_c$ range, the system exhibits a rather unusual feature. One may see in the zoomed plot of Fig. 5.1, that the low temperature FOT (dashed green curve which starts at the point C) splits, at an intermediate temperature (point J), into an upper SOT (solid green curve J-I) between the normal and the superconducting phase and into a lower

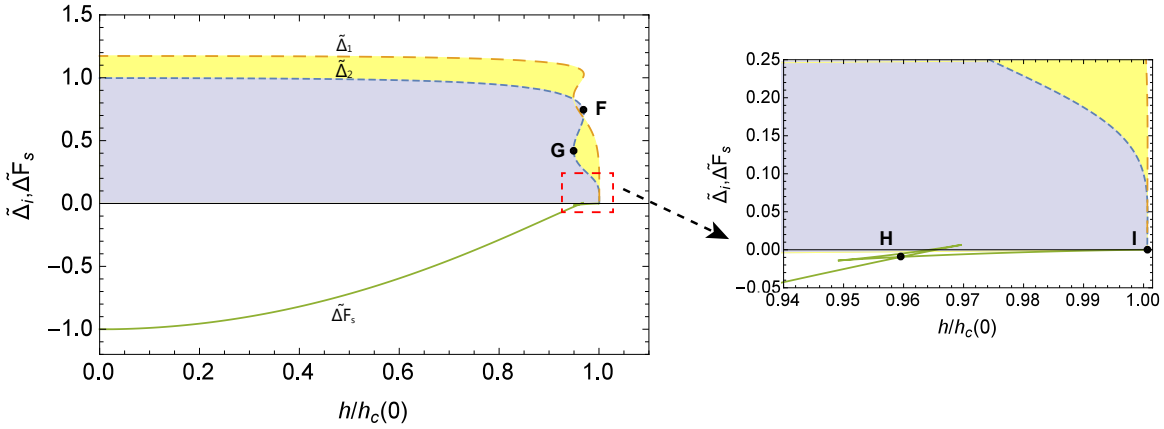

Figure 5.3: (a) Solutions of the coupled gap equations (normalized to the zero field value of band 1) and the total free energy difference between the superconducting and the normal phases (normalized to its zero field value) versus in-plane magnetic field (normalized to the zero temperature critical field) of a two-band intercalated graphite superconductor at $T = 0.26T_c$ for $V_{22} = 0.26$ and a zoomed region showing a crossing in the free energy before the SOT to the normal phase. The labeled points correspond to those in Fig. 5.1.

FOT (dashed green curve J-H) that reflects a transition between superconducting phases. This is understood as a consequence of the crossing of the metastability regions associated with the graphene-like band and the metallic band as the graphene-like intraband pairing interaction is increased. The bifurcation occurs because the metastability region of the graphene-like band is much narrower than that of the metallic band. These two transitions are not the continuation of the low temperature FOT. In fact, in this case, the SOT is the continuation of an additional supercooling field at low temperature (dashed blue curve which goes from the point E to J). We can confirm the splitting of the FOT by analyzing the band gap solutions and the free energy, for $T = 0.26T_c$, shown in Fig. 5.3. On one hand, the band gap solutions curves go smoothly to zero (point I) at large fields (i.e., a SOT occurs), but on the other hand, the crossing in the free energy (point H) occurs before the SOT between the superconductor and the normal phase (i.e., an additional FOT occurs).

It is expected that by increasing V_{22} even more, the superconducting phase diagram will finally change into a typical two-band superconductor phase diagram. Indeed, for $V_{22} = 0.26$, two FOTs (dashed green curves which start at C and F) and the two respective metastability regions (points A-B and D-E, respectively) are present at low temperature in the phase diagram, Fig. 5.1(c). One of them corresponds to the superconducting to normal transition (yellow shaded area) and is due to the graphene-like band and the other (blue shaded area) due to the metallic interlayer band corresponds to an FOT between different superconducting phases. The additional low temperature FOT between superconducting phases can be observed in the zero temperature band gap solutions, Fig. 5.2(i), where the crossing in the free energy, at the point C, occurs before it changes its sign, at the point F.

The profile change of the phase diagram from that of a one-band to that of a two-band

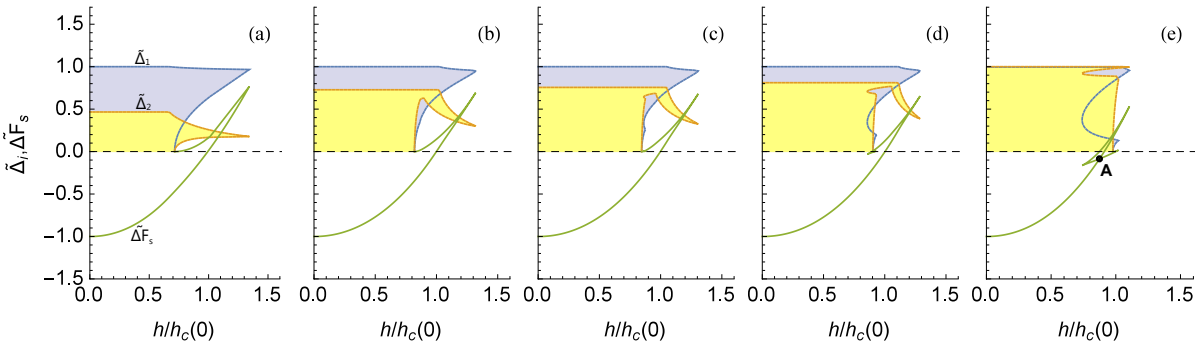

Figure 5.4: Zero temperature gap solutions (normalized to the zero field value of band 1) and the total free energy difference (normalized to its zero field value) versus in-plane magnetic field (normalized to the zero temperature critical field) for intercalated graphite for (a) $V_{22} = 0.26$, (b) $V_{22} = 0.262$, (c) $V_{22} = 0.266$, (d) $V_{22} = 0.268$ and (e) $V_{22} = 0.28$. Other parameters: $\mu/D = 0$, $V_{11} = 0.28$ and $V_{12} = 0.008$. Other parameters: $\mu/D = 0$, $V_{11} = 0.28$ and $V_{12} = 0.008$. In (c), a small additional reentrance arises in the gap solution curves, at the supercooling field associated to the metallic interlayer band. This reentrance widens as we increase V_{22}, and an additional FOT between superconducting phases occurs in (e), at point A.

superconductor due to the increase of V_{22} is shown in detail in Fig. 5.4(a)-(e) for, respectively, $V_{22} = 0.26$, $V_{22} = 0.262$, $V_{22} = 0.266$, $V_{22} = 0.268$ and $V_{22} = 0.28$, and fixed parameters $V_{11} = 0.028$ and $V_{12} = 0.008$. At $V_{22} = 0.266$ [Fig. 5.4(c)], a small reentrance appears in both gap solution curves and grows as we increase V_{22}. An additional FOT between superconducting phases occurs when $V_{22} = 0.28$ [Fig. 5.4(e) point A]. An interesting feature of these plots is that the additional reentrance arises at the supercooling field associated to the metallic interlayer band. This can be understood as a natural consequence of going from the gap curves of a one-band superconductor (which have only one reentrance at zero temperature, see Figs.5.4 (a),(b)) to the typical behavior of a two-band superconductor where the superconducting gaps show two reentrances at zero temperature [see Figs.5.4 (c),(d),(e)]. Furthermore, using a different V_{11} from the case of Fig.5.2, we show that V_{c2} depends on V_{11}. Comparing the values of V_{11} and V_{c2} between the case of Fig.5.2 [$V_{11} = 0.2$, $V_{c2} = 0.24$] with the one of Fig.5.4 [$V_{11} = 0.28$, $V_{c2} = 0.266$] one concludes that an increase on V_{11} leads to an increase of V_{c2}.

5.2.2 Dependence on the doping

We conclude that increasing V_{22} from $V_{22} < V_{c2}$ to $V_{22} > V_{c2}$ causes the system to behave as a typical two-band superconductor. Let us now consider what happens if we fix V_{22} and, instead, we dope the graphene layer. The zero temperature gap solutions for the $V_{22} = 0.18$, $V_{22} = 0.24$ and $V_{22} = 0.26$ cases for small doping, $\mu/D = 0.05$, intermediate doping, $\mu/D = 0.15$, and large doping, $\mu/D = 0.34$, are shown in Figs. 5.2(b)-(d), (f)-(h) and (j)-(l).

In the case of the left column [Figs. 5.2(a)-(d)], increasing μ allows for the appearance of the additional reentrance [see Fig. 5.2(c) points D-E]. However, the crossing in the free energy difference between the superconducting and the normal phase, at point F, occurs after it changes

its sign. For a large μ, Fig. 5.2(d), the system, finally, shows the additional transition between superconducting phases since the crossing in the free energy difference between the superconducting and the normal phase, at point G, occurs before it changes its sign. Thus, in this case, the phase diagram behaves as that of a typical two-band superconductor. In the case of the middle column [Figs. 5.2(e)-(h)], due to the fact that $V_{22} \gtrsim V_{c2}$, a small μ is enough to obtain a phase diagram as that of a two-band superconductor since one observes the appearance of the additional FOT [Fig. 5.2(f) point F]. In the case of the right column [Figs. 5.2(i)-(l)], one observes the increase of the metastability region width, associated to the graphene-like band, with increasing doping [Figs. 5.2(j)-(l)]. In general, doping the graphene-like band causes a change in the GICs phase diagram from a one-band superconductor-like to a two-band superconductor-like. Furthermore, when the metastability region associated with the graphene-like band is present, its normalized width increases with doping, a feature expected taking into account what we concluded in the previous section.

Chapter 6

Superconducting upper critical field in one-band metallic and semi-metallic superconductors

When magnetic fields are applied perpendicularly to the conducting planes of a quasi-2D superconductor the Zeeman pair breaking terms can be neglected and the orbital ones become dominant. In this case, the effect of the magnetic field can be studied using a semi-classic approach [46].

In this chapter, we start by introducing the Hamiltonian of a n-band superconductor under external perpendicular magnetic fields followed by a derivation of the coupled band gap equations. Next, we determine the pair propagator real space dependence for the cases of one-band metallic and semi-metallic superconductors. Finally, we show the dependence on temperature of the superconducting upper critical field, h_c.

6.1 n-band Hamiltonian and band gap equation

The Hamiltonian of a n-band 2D superconductor under perpendicular magnetic fields is given by

$$H = H_i + H_{int}, \tag{6.1}$$

with

$$\begin{aligned} H_i = \sum_i \{ & -\frac{1}{2m_i} \sum_\sigma \int \Psi^\dagger_{i\sigma}(\mathbf{r}t)[\nabla - ieA(\mathbf{r})]^2 \Psi_{i\sigma}(\mathbf{r}t) d\mathbf{r} \\ & - V_{ii} \int \Psi^\dagger_{i\uparrow}(\mathbf{r}t)\Psi^\dagger_{i\downarrow}(\mathbf{r}t)\Psi_{i\downarrow}(\mathbf{r}t)\Psi_{i\uparrow}(\mathbf{r}t) d\mathbf{r}\}, \end{aligned} \tag{6.2}$$

$$H_{int} = \sum_{i \neq j} [-V_{ij} \int \Psi^\dagger_{i\uparrow}(\mathbf{r}t)\Psi^\dagger_{i\downarrow}(\mathbf{r}t)\Psi_{j\downarrow}(\mathbf{r}t)\Psi_{j\uparrow}(\mathbf{r}t) d\mathbf{r} + H.c.], \tag{6.3}$$

where i, j label the bands, m_i is the mass of i-band electrons, and $\Psi^{\dagger}_{i\sigma}(\mathbf{r}t)[\Psi_{i\sigma}(\mathbf{r}t)]$ creates (annihilates) a i-band electron with spin σ. V_{ii} and V_{ij} are again the intraband and interband pairing interactions, respectively.

From this Hamiltonian, in the case of a one-band system, one obtains the usual differential equations for the Green's functions in real space, defined by Abrikosov *et al* [47], and these equations remain unchanged in the case of a n-band system [48] (with a generalized expression for the gap functions) and are given by

$$(i\omega+\frac{1}{2m}[\nabla_r-ie\mathbf{A}(\mathbf{r})]^2+\mu)\mathscr{G}^{HS}_{i,\omega}(\mathbf{r},\mathbf{r}')+\int d\tilde{\mathbf{r}}\Delta_i(\mathbf{r},\tilde{\mathbf{r}})\mathscr{F}^{\dagger}_{i,\omega}(\tilde{\mathbf{r}},\mathbf{r}')=\delta(\mathbf{r}-\mathbf{r}'), \tag{6.4}$$

$$(-i\omega+\frac{1}{2m}[\nabla_r+ie\mathbf{A}(\mathbf{r})]^2+\mu)\mathscr{F}^{\dagger}_{i,\omega}(\mathbf{r},\mathbf{r}')-\int d\tilde{\mathbf{r}}\Delta^*_i(\mathbf{r},\tilde{\mathbf{r}})\mathscr{G}^{HS}_{i,\omega}(\tilde{\mathbf{r}},\mathbf{r}')=0, \tag{6.5}$$

where $\mathscr{F}^{\dagger}_{i,\omega}$ is the anomalous Green's function and the Green's function $\mathscr{G}^{HS}_{i,\omega}$ describes the superconducting state in a magnetic field and where the energy gap, Δ^*_i, in a n-band system, is given by:

$$\Delta^*_i(\mathbf{r},\mathbf{r})=k_BT[V_{ii}\mathscr{F}^{\dagger}_{i,\omega}(\mathbf{r},\mathbf{r})+\sum_{j\neq i}V_{ij}\mathscr{F}^{\dagger}_{j,\omega}(\mathbf{r},\mathbf{r})]. \tag{6.6}$$

The normal state Green's function $\mathscr{G}^{H}_{i,\omega}$ satisfies the following equation

$$(i\omega+\frac{1}{2m}[\nabla_r+ie\mathbf{A}(\mathbf{r})]^2+\mu)\mathscr{G}^{H}_{i,\omega}(\mathbf{r},\mathbf{r}')=\delta(\mathbf{r}-\mathbf{r}'), \tag{6.7}$$

which can be written as

$$(i\omega+\frac{1}{2m}[\nabla_{r'}+ie\mathbf{A}(\mathbf{r}')]^2+\mu)\mathscr{G}^{H}_{i,\omega}(\mathbf{r},\mathbf{r}')=\delta(\mathbf{r}-\mathbf{r}'). \tag{6.8}$$

Using Eq. 6.8, Eqs. 6.4 and 6.5 can be rewritten into

$$\mathscr{G}^{HS}_{i,\omega}(\mathbf{r},\mathbf{r}')=\mathscr{G}^{H}_{i,\omega}(\mathbf{r},\mathbf{r}')-\int d\tilde{\mathbf{r}}d\mathbf{l}\mathscr{G}^{H}_{i,\omega}(\mathbf{r},\mathbf{l})\Delta_i(\mathbf{l},\tilde{\mathbf{r}})\mathscr{F}^{\dagger}_{i,\omega}(\tilde{\mathbf{r}},\mathbf{r}'), \tag{6.9}$$

$$\mathscr{F}^{\dagger}_{i,\omega}(\mathbf{r},\mathbf{r}')=\int d\tilde{\mathbf{r}}d\mathbf{l}\mathscr{G}^{H}_{i,-\omega}(\mathbf{l},\mathbf{r})\Delta^*_i(\mathbf{l},\tilde{\mathbf{r}})\mathscr{G}^{HS}_{i,\omega}(\tilde{\mathbf{r}},\mathbf{r}'). \tag{6.10}$$

Since the gap parameter is very small in the vicinity of the upper critical transition curve, one can expand $\mathscr{F}^{\dagger}_{i,\omega}(\mathbf{r},\mathbf{r})$ in powers of Δ. In order to obtain the band gap equation one must linearize Eq. 6.10, replace $\mathscr{G}^{HS}_{i,\omega}$ by $\mathscr{G}^{H}_{i,\omega}$ and substitute it in Eq. 6.6.

Note that in the absence of magnetic field, the gap function only depends on the relative position of the pair, i.e., $\Delta(\mathbf{r},\mathbf{r}') \to \Delta(\mathbf{r}-\mathbf{r}')$. In the particular case of a local pairing interaction, $V(\mathbf{r}-\mathbf{r}') = V\delta(\mathbf{r}-\mathbf{r}')$, one obtains the usual s-wave gap function, $\Delta(\mathbf{r},\mathbf{r}') = \Delta\delta(\mathbf{r}-\mathbf{r}')$. In the presence of a magnetic field

$$\Delta(\mathbf{r},\mathbf{r}') = \Delta(\mathbf{r})\delta(\mathbf{r}-\mathbf{r}'). \tag{6.11}$$

Thus, the band gap equation becomes

$$\Delta_i(\mathbf{r}) = V_{ii}\int d\mathbf{r}' K^H_{\beta i}(\mathbf{r}',\mathbf{r})\Delta_i(\mathbf{r}') + \sum_{j\neq i} V_{ij}\int d\mathbf{r}' K^H_{\beta j}(\mathbf{r}',\mathbf{r})\Delta_j(\mathbf{r}'), \tag{6.12}$$

where $K^H_{\beta i}(\mathbf{r}',\mathbf{r})$ is the pair propagator and is defined by

$$K^H_{\beta i}(\mathbf{r}',\mathbf{r}) = \frac{1}{\beta}\sum_{\omega} \mathscr{G}^H_{i,-\omega}(\mathbf{r}',\mathbf{r})\mathscr{G}^H_{i\omega}(\mathbf{r}',\mathbf{r}). \tag{6.13}$$

Under the semi-classic approximation [47]

$$K^H_{\beta i}(\mathbf{r}',\mathbf{r}) = K_{\beta i}(\mathbf{r}'-\mathbf{r})e^{(i\frac{2e}{\hbar c}\mathbf{A}(\mathbf{r})\cdot(\mathbf{r}'-\mathbf{r}))}, \tag{6.14}$$

where $K_{\beta i}(\mathbf{r})$ is the fermion pair propagator in real space at a temperature $k_BT = 1/\beta$, in the absence of external fields, intraband and interband pairing interactions. Then, the superconducting transition for a 2D system in an external magnetic field can be described by the semi-classical linearized gap equation

$$\begin{aligned}\Delta_i(\mathbf{r}) = {} & V_{ii}\int d\mathbf{r}' K_{\beta i}(\mathbf{r}')e^{i2\mathbf{A}(\mathbf{r})\cdot(\mathbf{r}'-\mathbf{r})}\Delta_i(\mathbf{r}+\mathbf{r}') \\ & + \sum_{j\neq i} V_{ij}\int d\mathbf{r}' K_{\beta j}(\mathbf{r}')e^{i2\mathbf{A}(\mathbf{r})\cdot(\mathbf{r}'-\mathbf{r})}\Delta_j(\mathbf{r}+\mathbf{r}'),\end{aligned} \tag{6.15}$$

where the geometrized unit system, i.e., $\hbar = c = e = k_B = \mu_B = 1$, was used.

For 2D, Eq. 6.15 in the symmetric gauge $\mathbf{A} = \frac{1}{2}\mathbf{H}\times r$ becomes

$$\Delta_i(\mathbf{r}) = V_{ii}\int d\mathbf{r}' K_{\beta i}(\mathbf{r}')e^{i\frac{\mathbf{r}\times\mathbf{r}'}{l^2}}\Delta_i(\mathbf{r}+\mathbf{r}') + \sum_j V_{ij}\int d\mathbf{r}' K_{\beta j}(\mathbf{r}')e^{i\frac{\mathbf{r}\times\mathbf{r}'}{l^2}}\Delta_j(\mathbf{r}+\mathbf{r}') \tag{6.16}$$

where l is related to the magnetic field by $H = \phi_0(2\pi l^2)^{-1}$ where ϕ_0 is the flux quantum hc/e. Eq. 6.16 has, in the case of an isotropic metallic band, as pointed out by Rajagopal and Vasudevan [49], a solution of the form

$$\Delta(r) = \Delta e^{-\frac{1}{2}(\frac{r}{l})^2}, \tag{6.17}$$

and we will assume a solution of this form in the case of a isotropic semi-metallic band.

Finally, substituting Eq. 6.17 into Eq. 6.16, one obtains the band gap solutions for the case of an isotropic 2D n-band superconductor

$$\Delta_i(r) = 2\pi \left(V_{ii} \int_{r_0}^{\infty} K_{\beta_i}(r) e^{-\frac{r^2}{2l^2}} \Delta_i r dr + \sum_j V_{ij} \int_{r_0}^{\infty} K_{\beta_i}(r) e^{-\frac{r^2}{2l^2}} \Delta_j r dr \right), \tag{6.18}$$

where r_0 is a lower cutoff (equivalent to a high momentum cutoff).

6.2 Pair propagator for a isotropic 2D one-band superconductor

The pair propagator for a isotropic 2D one-band superconducting can be obtained by using Eq. 6.13. In order to determine the real space Green's functions, $\mathscr{G}_{\omega}(\mathbf{r})$ and $\mathscr{G}_{-\omega}(\mathbf{r})$, one can make a 2D Fourier transform of the respective Green's functions in the momentum space, $\mathscr{G}_{\omega}(\mathbf{k})$ and $\mathscr{G}_{-\omega}(\mathbf{k})$,

$$\mathscr{G}_{\pm\omega}(\mathbf{r}) = \frac{1}{4\pi^2} \int d\mathbf{k} e^{i\mathbf{k}.\mathbf{r}} \mathscr{G}_{\pm\omega}(\mathbf{k}), \tag{6.19}$$

where

$$\mathscr{G}_{\pm\omega}(\mathbf{k}) = \frac{1}{\pm i\omega - \varepsilon_{\mathbf{k}}}. \tag{6.20}$$

Due to the isotropic nature of the superconductors under consideration, one has

$$\mathscr{G}_{\pm\omega}(\mathbf{r}) \to \mathscr{G}_{\pm\omega}(r) \tag{6.21a}$$

$$\mathscr{G}_{\pm\omega}(\mathbf{k}) \to \mathscr{G}_{\pm\omega}(k) \tag{6.21b}$$

and one can write

$$\mathscr{G}_{\pm\omega}(r) = \frac{1}{4\pi^2} \int_0^{2\pi} d\phi \int_0^{\infty} dk k e^{ikr\cos(\phi)} \mathscr{G}_{\pm\omega}(k). \tag{6.22}$$

Since

$$\int_0^{2\pi} d\phi e^{ikr\cos(\phi)} = 2\pi J_0(kr), \tag{6.23}$$

Eq. 6.22 becomes

$$\mathscr{G}_{\pm\omega}(r) = \frac{1}{2\pi} \int_0^{\infty} dk k J_0(qr) \mathscr{G}_{\pm\omega}(k), \tag{6.24}$$

and using the approximations

$$k \approx k_F, \tag{6.25}$$

and

$$\begin{aligned} J_0(kr) &\approx \sqrt{\frac{2}{\pi kr}}\cos(kr-\frac{\pi}{4}) \\ &= \sqrt{\frac{2}{\pi kr}}\frac{e^{i(-\frac{\pi}{4})}e^{ikr}+e^{-i(-\frac{\pi}{4})}e^{-ikr}}{2}, \end{aligned} \tag{6.26}$$

one gets

$$\begin{aligned} \mathscr{G}_{\pm\omega}(r) = \frac{1}{4\pi}\sqrt{\frac{2k_F}{\pi r}}\Bigg\{ & e^{i(-\frac{\pi}{4})}\int_0^\infty dk e^{ikr}\mathscr{G}_{\pm\omega}(k) \\ & + e^{-i(-\frac{\pi}{4})}\int_0^\infty dk e^{-ikr}\mathscr{G}_{\pm\omega}(k)\Bigg\}. \end{aligned} \tag{6.27}$$

By doing a variable change, such that

$$q = k - k_F, \tag{6.28a}$$

$$dq = dk, \tag{6.28b}$$

one obtains

$$\begin{aligned} \mathscr{G}_{\pm\omega}(r) = & \frac{1}{4\pi}\sqrt{\frac{2k_F}{\pi r}} \\ & \left\{ e^{i(k_F r-\frac{\pi}{4})}\int_{-\infty}^\infty dq e^{iqr}\mathscr{G}_{\pm\omega}(q) + e^{-i(k_F r-\frac{\pi}{4})}\int_{-\infty}^\infty dq e^{-iqr}\mathscr{G}_{\pm\omega}(q)\right\}, \end{aligned} \tag{6.29}$$

where the integral over q was extended such that $\int_{-k_F}^\infty dq \to \int_{-\infty}^\infty dq$.

Going back to Eq. 6.13, and dropping fast oscillating terms from the product $\mathscr{G}_\omega(r)\mathscr{G}_{-\omega}(r)$, one can write

$$\begin{aligned} K_\beta(\mathbf{r}) &= \frac{1}{\beta}\sum_\omega \mathscr{G}_\omega(\mathbf{r})\mathscr{G}_{-\omega}(\mathbf{r}) \\ &\approx \frac{1}{\beta}\sum_\omega \left(\frac{1}{4\pi}\sqrt{\frac{2k_F}{\pi r}}\right)^2 \\ &\quad \times \Bigg\{ \int_{-\infty}^\infty dq_1 e^{iq_1 r}\mathscr{G}_\omega(q_1)\int_{-\infty}^\infty dq_2 e^{-iq_2 r}\mathscr{G}_{-\omega}(q_2) \\ &\quad + \int_{-\infty}^\infty dq_1 e^{-iq_1 r}\mathscr{G}_\omega(q_1)\int_{-\infty}^\infty dq_2 e^{iq_2 r}\mathscr{G}_{-\omega}(q_2)\Bigg\}. \end{aligned} \tag{6.30}$$

where the sum is done over

$$\omega_n = (2n+1)\frac{\pi}{\beta}, \tag{6.31}$$

with $n = ..., -2, -1, 0, 1, 2, ...$

Since the product $\mathscr{G}_{\omega}(r)\mathscr{G}_{-\omega}(r)$ is even in ω, one has

$$\sum_{\omega_n} \to 2\sum_{n=0}^{\infty} \tag{6.32}$$

and one finally obtains the pair propagator for a isotropic 2D one-band superconductor,

$$\begin{aligned} K_{\beta}(r) &= \frac{2}{\beta}\sum_{n=0}^{\infty}\mathscr{G}_{\omega}(r)\mathscr{G}_{-\omega}(r) \\ &= \frac{1}{\beta}\left(\frac{1}{8\pi^2}\right)\left(\frac{2k_F}{\pi r}\right)\sum_{n=0}^{\infty} \quad \left\{\int_{-\infty}^{\infty} dq_1 e^{iq_1 r}\mathscr{G}_{\omega_n}(q_1)\int_{-\infty}^{\infty} dq_2 e^{-iq_2 r}\mathscr{G}_{-\omega_n}(q_2)\right. \\ &\quad \left. + \int_{-\infty}^{\infty} dq_1 e^{-iq_1 r}\mathscr{G}_{\omega_n}(q_1)\int_{-\infty}^{\infty} dq_2 e^{iq_2 r}\mathscr{G}_{-\omega_n}(q_2)\right\}. \end{aligned} \tag{6.33}$$

6.2.1 Pair propagator for a isotropic 2D one-band metallic superconductor

We use now Eq. 6.33 to determine the pair propagator for a isotropic 2D one-band metallic superconductor. The momentum Green's functions are, in the case of a metallic band with constant density of states, given by

$$\mathscr{G}_{\pm\omega}(q) = \frac{1}{\pm i\omega - v_F q}. \tag{6.34}$$

Below, Eq. 6.33 integrals are calculated. The first and the second ones are given by

$$\begin{aligned} \int_{-\infty}^{\infty} dq_1 e^{iq_1 r}\mathscr{G}_{\omega}(q_1) &= \int_{-\infty}^{\infty} dq_1 e^{iq_1 r}\frac{1}{i\omega - v_F q_1} \\ &= \int_{-\infty}^{\infty} dq_1 \left(\frac{e^{iq_1 r}}{-v_F}\right)\left(\frac{1}{q_1 - \frac{i\omega}{v_F}}\right) \\ &= 2\pi i\frac{e^{-\frac{\omega r}{v_F}}}{(-v_F)}\Theta(\omega), \end{aligned} \tag{6.35}$$

$$\begin{aligned} \int_{-\infty}^{\infty} dq_2 e^{-iq_2 r}\mathscr{G}_{-\omega}(q_2) &= \int_{-\infty}^{\infty} dq_2 e^{-iq_2 r}\frac{1}{-i\omega - v_F q_2} \\ &= \int_{-\infty}^{\infty} dq_2 \left(\frac{e^{-iq_2 r}}{-v_F}\right)\left(\frac{1}{q_2 + \frac{i\omega}{v_F}}\right) \\ &= -2\pi i\frac{e^{-\frac{\omega r}{v_F}}}{(-v_F)}\Theta(\omega). \end{aligned} \tag{6.36}$$

The third and fourth can be obtained by doing $\omega \to -\omega$ and comparing with Eqs. 6.36 and 6.35, respectively

$$\begin{aligned}\int_{-\infty}^{\infty} dq_1 e^{-iq_1 r}\mathscr{G}_{\omega}(q_1) &= \int_{-\infty}^{\infty} dq_1 e^{-iq_1 r}\frac{1}{i\omega - v_F q_1} \\ &= -2\pi i\frac{e^{\frac{\omega r}{v_F}}}{(-v_F)}\Theta(-\omega),\end{aligned} \tag{6.37}$$

$$\begin{aligned}\int_{-\infty}^{\infty} dq_2 e^{iq_2 r}\mathscr{G}_{-\omega}(q_2) &= \int_{-\infty}^{\infty} dq_2 e^{iq_2 r}\frac{1}{-i\omega - v_F q_2} \\ &= 2\pi i\frac{e^{\frac{\omega r}{v_F}}}{(-v_F)}\Theta(-\omega).\end{aligned} \tag{6.38}$$

Note that the two products of integrals of Eq. 6.33 are symmetric in ω, and since we are doing the sum over positive ω_n, we only consider the first product. Thus, one has

$$\begin{aligned}K_{\beta}(r) &= \frac{2}{\beta}\sum_{n=0}^{\infty}\mathscr{G}_{\omega_n}(r)\mathscr{G}_{-\omega_n}(r) \\ &= \frac{1}{\beta}\frac{1}{8\pi^2}\left(\frac{2k_F}{\pi r}\right)\left(\frac{4\pi^2}{v_F^2}\right)\sum_{n=0}^{\infty} e^{-2\frac{\omega_n r}{v_F}} \\ &= \frac{1}{\beta}\frac{k_F}{\pi v_F^2 r}\sum_{n=0}^{\infty} e^{-\frac{2r}{v_F}\frac{2\pi}{\beta}(n+\frac{1}{2})},\end{aligned} \tag{6.39}$$

where

$$\begin{aligned}\sum_{n=0}^{\infty} e^{-\frac{2r}{v_F}\frac{2\pi}{\beta}(n+\frac{1}{2})} &= e^{-\alpha/2}\frac{1}{1-e^{-\alpha}} \\ &= \frac{1}{\sinh(\alpha/2)},\end{aligned} \tag{6.40}$$

with $\alpha = \frac{4\pi r}{v_F\beta}$.

Finally, the pair propagator for a isotropic 2D one-band metallic superconductor is given by

$$K_{\beta}(r) = \frac{1}{\beta}\frac{k_F}{\pi v_F^2 r}\frac{1}{\sinh(\frac{2\pi r}{v_F\beta})}, \tag{6.41}$$

and substituting Eq. 6.41 into Eq. 6.18 (and doing $i = j = 1$), one obtains the equation that gives the dependence on temperature of the superconducting upper critical field.

$$\int_{r_0}^{\infty}\frac{1}{\beta}\frac{k_F}{\pi r v_F^2}\frac{e^{-\frac{r^2}{2l^2}}}{\sinh(\frac{2\pi r}{v_F\beta})}rdr = \frac{1}{2\pi V_{11}}. \tag{6.42}$$

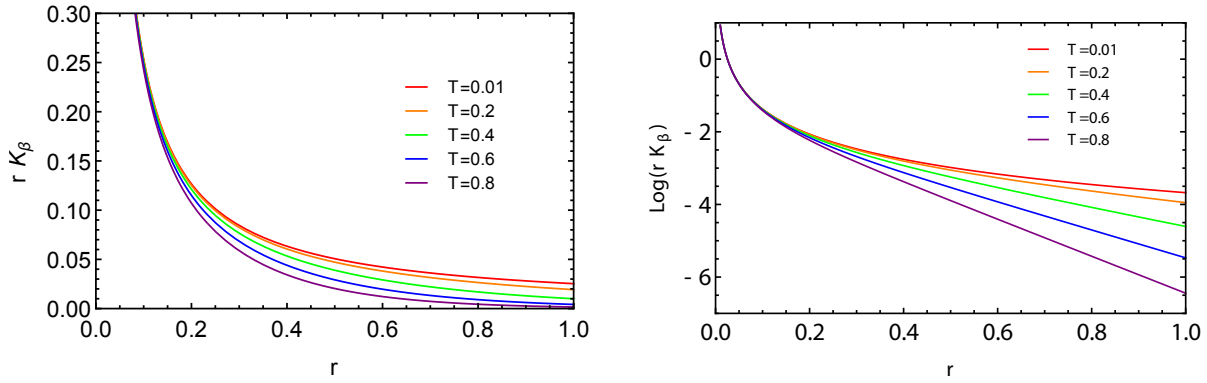

(a) (b)

Figure 6.1: (a) Pair propagator spacial dependence for a 2D isotropic superconducting metal, for several temperatures. The curves diverge as $r \to 0$ and decay as $r \to \infty$. (b) Pair propagator spacial dependence in a semi-logarithmic scale. The linear behaviour for large r implies a exponential decay of the pair propagator, for large r.

The zero field solution can be obtained by doing $h = 0$ $(1/l^2 = 0)$ in Eq. 6.42

$$\int_{r_0}^{\infty} \frac{k_F}{\pi v_F^2} \frac{T}{\sinh(\frac{2\pi r T}{v_F})} dr = \frac{1}{2\pi V_{11}}. \tag{6.43}$$

The real space dependence of the pair propagator, or more precisely, the expression in the integral of the left member of Eq. 6.43, $rK_\beta(r)$, is shown in Fig. 6.1a for several temperatures, for $v_F = k_F = 1$. The curves diverge at $r \to 0$ and decay as r increases. But one can ask, how fast these curves diverge and decay? And are these behaviours temperature dependent?

Analytically, one can expand $rK_\beta(r)$ [apart from constants, $rK_\beta(r) = \frac{T}{\sinh(rT)}$], for both small and large r. For small r, one has

$$\begin{aligned} \frac{T}{\sinh(rT)} &\approx \frac{T}{rT} \\ &= \frac{1}{r}. \end{aligned} \tag{6.44}$$

Thus, $rK_\beta(r)$ diverges as a temperature independent power-law. Looking to Fig. 6.1a, one observes that for small enough r all curves diverge similarly. These features can be perceived graphically from the $\log[rK_\beta(r)]$ *vs.* $\log(r)$ plot, shown at Fig. 6.2a. The linear behaviour of these curves, for small r, that is, $\log[rK_\beta(r)] = -a\log(r)$ leads to $rK_\beta(r) = r^{-a}$, where $a = 1$, and one gets $rK_\beta(r) \propto \frac{1}{r}$.

For large r, one has

$$\begin{aligned} \frac{T}{\sinh(rT)} &\approx \frac{T}{e^{rT}} \\ &= Te^{-Tr}. \end{aligned} \tag{6.45}$$

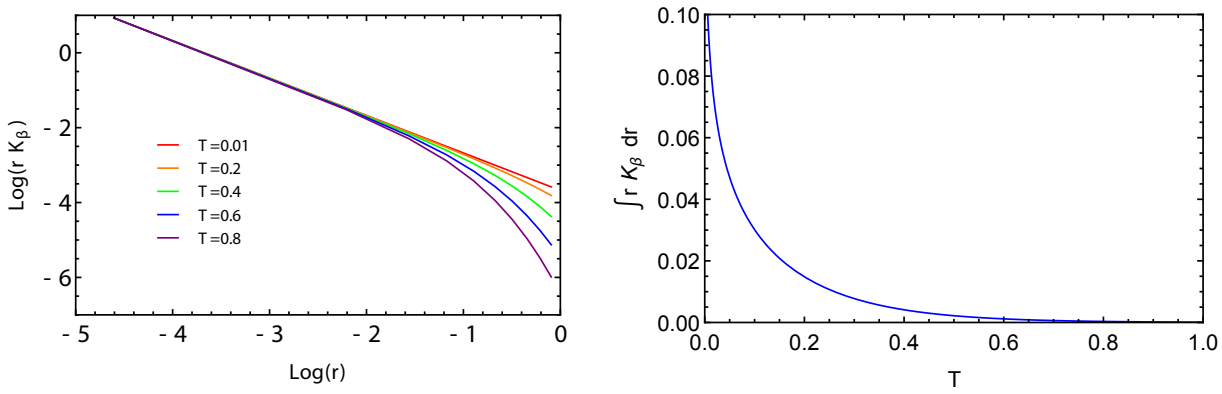

(a) (b)

Figure 6.2: (a) Pair propagator spacial dependence in a logarithmic scale. The curves behave linearly for small r, meaning that the pair propagator diverge as a power-law, for small r. (b) Temperature dependence of the left term of Eq. 6.42. The curve diverges as $T \to 0$, that is, there is a finite critical temperature for any finite metallic intraband interaction.

Then, $rK_\beta(r)$ decays as a temperature dependent exponential. In Fig. 6.1a one notices that $rK_\beta(r)$ decays faster, for large r, for larger temperatures. From the $\log[rK_\beta(r)]$ *vs.* r plot, shown at Fig. 6.1b, one can identify, for large r, a linear behaviour, $\log[rK_\beta(r)] = -ar$, which leads to a exponential decay $rK_\beta(r) = e^{-ar}$. However, in this case, the slope of the curve increases with temperature, meaning, as we concluded analytically, that $rK_\beta(r)$ decays faster for larger temperatures.

In order to determine T_c, one solves the zero field equation, Eq. 6.43. Solving the integral, one obtains

$$-\alpha_1 \log\left[\tanh\left(\frac{\pi r_0 T_c}{v_F}\right)\right] = \frac{1}{V}, \tag{6.46}$$

where $\alpha_1 = \frac{k_F}{\pi v_F}$.

Since r_0 is small, and $\tanh(x) \approx x$ for small x, Eq. 6.46 becomes

$$-\alpha_1 \log\left(\frac{\pi r_0 T_c}{v_F}\right) = \frac{1}{V}. \tag{6.47}$$

Finally, from Eq. 6.47 one obtains

$$T_c \propto e^{-\frac{1}{\alpha_1 V}}. \tag{6.48}$$

which is nothing more but the mean-field BCS theory expression for the critical temperature [recall Eq. 2.2]. From this equation, one concludes that there is a critical temperature for any finite metallic intraband interaction, as we pointed out already. This can be perceived graphically by plotting both terms of Eq. 6.43. For arbitrary small interactions, $\frac{1}{V} \to \infty$, the second member diverges (and tends to 0 as $V \to \infty$). Thus, in order to always find a solution for Eq. 6.43, the pair propagator, or more precisely, the left member of Eq. 6.43 should diverge for $T \to 0$, as one sees in Fig. 6.2b.

In order to determine the superconducting upper critical field, h_c, one solves Eq. 6.42 for $T = 0$, that is, one solves the zero temperature band gap equation

$$\int_{r_0}^{\infty} \frac{k_F}{\pi r v_F^2} \frac{T_0}{\sinh(\frac{2\pi r T_0}{v_F})} e^{-\frac{r^2}{2l_0^2}} r dr = \frac{1}{2\pi V}, \tag{6.49}$$

where $T_0 \to 0$.

Since $\sinh(x) \simeq x$ for small x, Eq. 6.49 becomes

$$\int_{r_0}^{\infty} \frac{k_F}{2\pi^2 v_F} \frac{1}{r} e^{-\frac{r^2}{2l_0^2}} dr = \frac{1}{2\pi V}. \tag{6.50}$$

Solving the integral, one obtains

$$-\frac{1}{2}\alpha_1 Ei\Big[-\frac{h_c \pi}{\phi_0} r_0^2\Big] = \frac{1}{V}. \tag{6.51}$$

Again by using the fact that r_0 is small, Eq. 6.51 becomes

$$-\frac{1}{2}\alpha_1 \log\Big(\frac{h_c \pi}{\phi_0} r_0^2 + \gamma\Big) = \frac{1}{V}, \tag{6.52}$$

where γ is the Euler-Mascheroni constant.

From 6.52, one gets

$$h_c \propto e^{-\frac{2}{\alpha_1 V}}. \tag{6.53}$$

From Eqs. 6.48 and 6.53 one obtains the usual BCS relation between T_c and h_c

$$h_c \propto T_c^2. \tag{6.54}$$

Using again Eq. 6.42, one can obtain the out-of-plane magnetic field *vs.* temperature phase diagram, shown in Fig. 6.3, for $V = 0.2$. The superconducting critical magnetic field decreases with temperature as a BCS curve, i.e., as a parabolic-like curve.

6.2.2 Pair propagator for a isotropic 2D one-band semi-metallic superconductor

In order to determine the pair propagator for a isotropic 2D one-band semi-metallic superconductor, we use once again Eq. 6.33 but this time considering a semi-metallic energy dispersion, $\varepsilon_k = v_F \sqrt{|q|}\,\mathrm{sign}(q)$ (which corresponds to a DOS that goes linearly to zero at the Fermi energy). However, in this case, the Fourier transform of the Green's functions are complex. In order to simplify the problem, we start by changing the order between the sums and the integrals

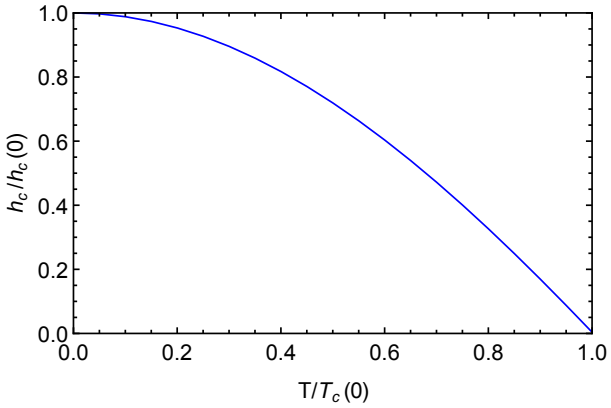

Figure 6.3: Upper critical field (normalized to its value at zero temperature) as function of temperature (normalized to the zero field critical temperature), for $V = 0.2$, for a metallic superconductor. The superconducting magnetic field decreases with temperature as a parabolic-like curve.

in Eq. 6.33, such that

$$K_\beta(r) = \frac{1}{2\beta}\frac{1}{8\pi^2}\left(\frac{2k_F}{\pi r}\right)\left\{\int_{-\infty}^{\infty} dq_1 e^{iq_1 r}\int_{-\infty}^{\infty} dq_2 e^{-iq_2 r}\sum_{\omega_n}\mathcal{G}(q_1,\omega_1)\mathcal{G}(q_2,-\omega_n) + \int_{-\infty}^{\infty} dq_1 e^{-iq_1 r}\int_{-\infty}^{\infty} dq_2 e^{iq_2 r}\quad\sum_{\omega_n}\mathcal{G}(q_1,\omega_n)\mathcal{G}(q_2,-\omega_n)\right\}, \tag{6.55}$$

and grouping the terms in q, Eq. 6.55 becomes

$$\begin{aligned} K_\beta(r) &= \frac{1}{2\beta}\frac{1}{8\pi^2}\left(\frac{2k_F}{\pi r}\right)\left\{\int_{-\infty}^{\infty} dq_1\int_{-\infty}^{\infty} dq_2\right. \\ &\left.\left[e^{i(q_1-q_2)r}+e^{-i(q_1-q_2)r}\right]\sum_{\omega_n}\mathcal{G}(q_1,\omega_n)\mathcal{G}(q_2,-\omega_n)\right\} \\ &= \frac{1}{\beta}\frac{1}{8\pi^2}\left(\frac{2k_F}{\pi r}\right)\left\{\int_{-\infty}^{\infty} dq_1\int_{-\infty}^{\infty} dq_2\cos(q_1-q_2)r\sum_{\omega_n}\mathcal{G}(q_1,\omega_n)\mathcal{G}(q_2,-\omega_n)\right\}. \end{aligned} \tag{6.56}$$

Using the result (from [50])

$$-\frac{1}{\beta}\sum_{\omega_n}\mathcal{G}(q_1,\omega_n)\mathcal{G}(q_2,-\omega_n) = \frac{1-n_F(\varepsilon_{q_1})-n_F(\varepsilon_{q_2})}{-\varepsilon_{q_1}-\varepsilon_{q_2}}, \tag{6.57}$$

one has

$$K_\beta(r) = \frac{1}{8\pi^2}\left(\frac{2k_F}{\pi r}\right)\left\{\int_{-\infty}^{\infty} dq_1\int_{-\infty}^{\infty} dq_2\cos\left[(q_1-q_2)r\right]\frac{1-n_F(\varepsilon_{q_1})-n_F(\varepsilon_{q_2})}{\varepsilon_{q_1}+\varepsilon_{q_2}}\right\}, \tag{6.58}$$

with

$$n_F(\varepsilon_{q_1}) = \frac{1}{e^{\beta\varepsilon_{q_1}}+1}, \tag{6.59a}$$

$$n_F(\varepsilon_{q_2}) = \frac{1}{e^{\beta\varepsilon_{q_2}}+1}. \tag{6.59b}$$

Eq. 6.58 can be simplified, by doing the following variable change,

$$\tilde{q}_1 = q_1 r, \tag{6.60a}$$

$$\tilde{q}_2 = q_2 r, \tag{6.60b}$$

to

$$rK_\beta(r) = \alpha_2 \int_{-\infty}^{\infty} \frac{d\tilde{q}_1}{r} \int_{-\infty}^{\infty} \frac{d\tilde{q}_2}{r} \cos(\tilde{q}_1 - \tilde{q}_2) \frac{1 - n_F(\varepsilon_{\tilde{q}_1/r}) - n_F(\varepsilon_{\tilde{q}_2/r})}{\varepsilon_{\tilde{q}_1/r} + \varepsilon_{\tilde{q}_2/r}}, \tag{6.61}$$

where $\alpha_2 = \frac{1}{8\pi^2}(\frac{2k_F}{\pi})$.

In order to ascertain the validity of Eq. 6.61, we use it, first, to study the pair propagator of a metallic band and compare with the results of the previous section. In the case of a metallic band, one has $\varepsilon_q = v_F q \Leftrightarrow \varepsilon_{\tilde{q}/r} = v_F \tilde{q}/r = \varepsilon_{\tilde{q}}/r$, and so, one can write

$$\begin{aligned} rK_\beta(r) &= \frac{\alpha_2}{r} \int_{-\infty}^{\infty} d\tilde{q}_1 \int_{-\infty}^{\infty} d\tilde{q}_2 \cos(\tilde{q}_1 - \tilde{q}_2) \frac{1 - \frac{1}{e^{\frac{\beta\varepsilon_{\tilde{q}_1}}{r}}+1} - \frac{1}{e^{\frac{\beta\varepsilon_{\tilde{q}_2}}{r}}+1}}{\varepsilon_{\tilde{q}_1} + \varepsilon_{\tilde{q}_2}} \\ &= \frac{\alpha_2}{r} F\left(\frac{r}{\beta}\right), \end{aligned} \tag{6.62}$$

which is consistent with

$$\begin{aligned} rK_\beta(r) &= \frac{k_F}{\pi v_F^2} r \frac{r}{\beta} \frac{1}{\sinh(\frac{2\pi r}{v_F \beta})} \\ &= \frac{k_F}{\pi v_F^2 r} F\left(\frac{r}{\beta}\right). \end{aligned} \tag{6.63}$$

In the case of a semi-metallic band one has $\varepsilon_q = v_F \sqrt{|q|}\,\mathrm{sign}(q) \Leftrightarrow \varepsilon_{\tilde{q}/r} = v_F \sqrt{|\tilde{q}|}\,\mathrm{sign}(\tilde{q})/\sqrt{r} = \varepsilon_{\tilde{q}}/\sqrt{r}$, and so, one can write

$$\begin{aligned} rK_\beta(r) &= \frac{\alpha_2}{r^2} \sqrt{r} \int_{-\infty}^{\infty} d\tilde{q}_1 \int_{-\infty}^{\infty} d\tilde{q}_2 \cos(\tilde{q}_1 - \tilde{q}_2) \frac{1 - \frac{1}{e^{\frac{\beta\varepsilon_{\tilde{q}_1}}{\sqrt{r}}}+1} - \frac{1}{e^{\frac{\beta\varepsilon_{\tilde{q}_2}}{\sqrt{r}}}+1}}{\varepsilon_{\tilde{q}_1} + \varepsilon_{\tilde{q}_2}} \\ &= \frac{\alpha_2}{r^{3/2}} F\left(\frac{\sqrt{r}}{\beta}\right). \end{aligned} \tag{6.64}$$

Then, in order to determine the pair propagator one only needs to know $F(x)$,

$$F(x) = \int_{-\infty}^{\infty} d\tilde{q}_1 \int_{-\infty}^{\infty} d\tilde{q}_2 \cos(\tilde{q}_1 - \tilde{q}_2) \frac{1 - \frac{1}{e^{\frac{\varepsilon_{\tilde{q}_1}}{x}}+1} - \frac{1}{e^{\frac{\varepsilon_{\tilde{q}_1}}{x}}+1}}{\varepsilon_{\tilde{q}_1} + \varepsilon_{\tilde{q}_1}}. \tag{6.65}$$

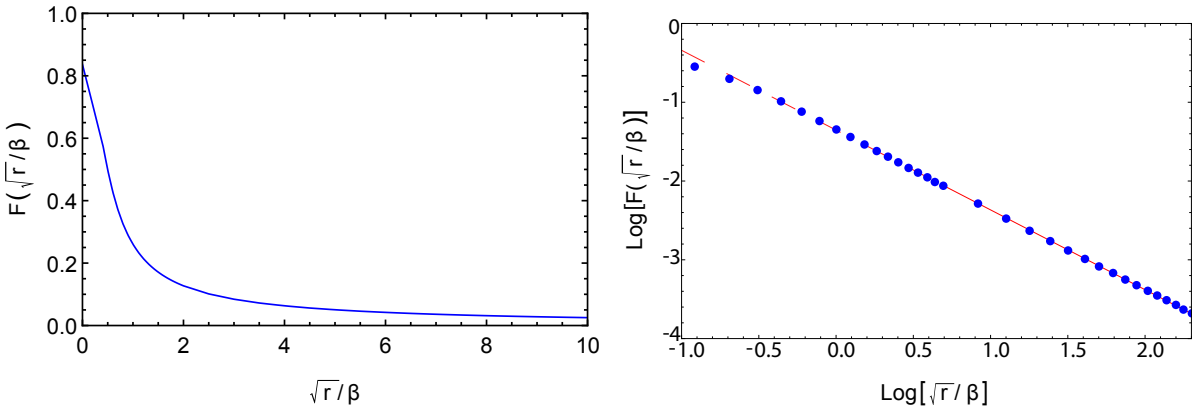

(a) (b)

Figure 6.4: (a) $F(x)$ dependence on x, for a semi-metallic superconductor, where $x = \sqrt{r}/\beta$. In the limit $x \to 0$, $F(x)$ is constant, and decays as a power-law for large x. (b) $F(x)$ dependence on x in a logarithmic scale. The function (blue points) behaves linearly (see red curve fit) for large x, meaning that the $F(x)$ decays as a power-law, for large x.

In the case of a metallic band, we know that

$$\lim_{x\to 0} F(x) = const. \tag{6.66}$$

We argue that this is also valid in the case of the semi-metallic band because, numerically, we do not see any divergence for $x = 0$ [see Fig. 6.4a] (note that in the numerical calculations we truncate the integrals, that is, we introduce a large q cutoff, but we studied the evolution of the integral when the cutoff was increased). In addition, we know that the integral $F(x = 0)$ is of the form

$$\int_{-\infty}^{\infty} dq_1 \int_{-\infty}^{\infty} dq_2 \cos(q_1 - q_2) \frac{1}{\varepsilon_{q_1} + \varepsilon_{q_2}}. \tag{6.67}$$

which, by using $\cos(q_1 - q_2) = \cos(q_1)\cos(q_2) + \sin(q_1)\sin(q_2)$, becomes

$$\int_{-\infty}^{\infty} dq_1 \cos(q_1) \int_{-\infty}^{\infty} dq_2 \cos(q_2) \frac{1}{\varepsilon_{q_1} + \varepsilon_{q_2}} + \int_{-\infty}^{\infty} dq_1 \sin(q_1) \int_{-\infty}^{\infty} dq_2 \sin(q_2) \frac{1}{\varepsilon_{q_1} + \varepsilon_{q_2}}. \tag{6.68}$$

and since the term in the fraction is a decaying function, as a power-law, of q_1 and q_2, the integrals converge, and consequently $F(x = 0)$ also converges.

Thus, we have

$$rK_\beta(r) = \frac{\alpha_2}{r} F\left(\frac{r}{\beta}\right) \tag{6.69}$$

with $\lim_{x\to 0} F(x) = \frac{v_F}{2\pi}$, for the metallic band, and

$$rK_\beta(r) = \frac{\alpha_2}{r^{3/2}} F\left(\frac{\sqrt{r}}{\beta}\right) \tag{6.70}$$

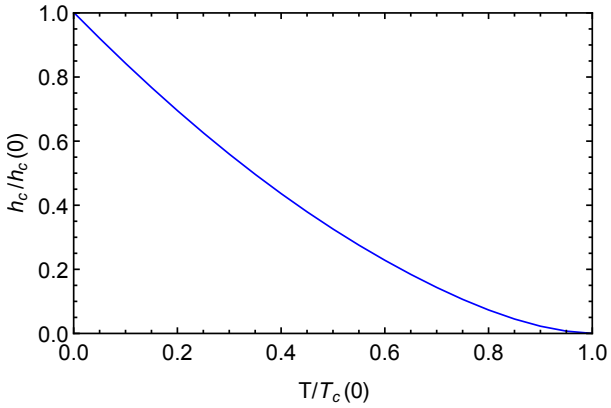

Figure 6.5: Upper critical field (normalized to its value at zero temperature) as function of temperature (normalized to the zero field critical temperature), for $V = 0.8$, for a semi-metallic superconductor. The temperature dependence of the superconducting magnetic field is described by a curve with positive curvature.

---

with $\lim_{x\to 0} F(x) = const$, for the semi-metallic band.

This implies a faster decay of $rK_\beta(r)$ for the semi-metallic band and in particular

$$\int_{r_0}^{\infty} rK_\beta(r)dr, \tag{6.71}$$

does not diverge as $T \to 0$. This means that there is a critical value of the pairing interaction in order for a superconducting phase to be present, in contrast with the case of a metallic band.

Numerically, from the $\log[F(x)]$ *vs.* $\log x$ plot, shown at Fig. 6.4b, where one sees that the function (blue points) behaves linearly [red curve fit] for large x, we have found that

$$\begin{aligned} F(x) &\propto \frac{1}{x}, \text{for } x > 1 \\ \Leftrightarrow F(\sqrt{r}/\beta) &\propto \frac{\beta}{\sqrt{r}}, \text{for } \sqrt{r} > \beta. \end{aligned} \tag{6.72}$$

So, one has

$$rK_\beta(r) = \frac{\alpha_2}{r^{3/2}} F\left(\frac{\sqrt{r}}{\beta}\right) = \begin{cases} \frac{\alpha_2}{r^{3/2}} const_1, & \sqrt{r} \ll \beta, \\ \frac{\alpha_2}{r^2}\beta const_2, & \sqrt{r} > \beta. \end{cases} \tag{6.73}$$

The out-of-plane magnetic field *vs.* temperature phase diagram for the case of a superconducting semi-metal band is shown at Fig. 6.5, for $V = 0.8$. In contrast with the parabolic curve of the phase diagram of a metallic band, we found that in the case of a semi-metal band the upper critical magnetic field displays a positive curvature.

Chapter 7

Conclusion

In this dissertation, we studied the phase diagram of one-band and two-band 2D superconductors with one semi-metallic band under parallel and perpendicular magnetic fields. Examples of systems with one semi-metallic band are graphene and GICs.

In particular, we studied metastability regions in the phase diagram of superconducting graphene and intercalated graphite superconductors under in-plane magnetic field both in doped and undoped cases, using a simple BCS multiband approach. In the case of a single undoped graphene band, a critical intraband interaction is required in order for a superconducting phase to be present in undoped graphene, but this critical intraband interaction vanishes for any finite doping. We showed that the introduction of doping in a graphene band also affects the behavior of the metastability region of the in-plane magnetic field *vs.* temperature phase diagram. The normalized area of the metastability region and the tricritical temperature value become smaller as doping goes to zero, contrasting with the case of a doped metallic band.

We have also studied the in-plane magnetic field *vs.* temperature phase diagram of a intercalated graphite superconductor, modeled as a two-dimensional two-band superconductor with one graphene-like band and a metallic interlayer band. In this case, finite interband pairing interactions imply the existence of a superconducting phase with finite superconducting gaps in both bands, that is, there is no critical intraband interaction for the graphene-like band. However, we found a new intraband critical interaction for the graphene-like band associated with the appearance of a second metastability region in the phase diagram. The phase diagrams obtained for a smaller and larger intraband interaction (of the graphene-like band) than the critical interaction are the ones of a typical one-band and two-band superconductor, respectively. When the intraband interaction of the graphene-like band is just slightly larger than this critical interaction, new features are observed in the phase diagram such as the absence of the low temperature first-order transition between superconducting phases and at an intermediate temperature, and the bifurcation of the low temperature first-order transition curve into a first-order transition between superconducting phases and a second-order transition between the normal and the superconducting phase. The second metastability region arises with increasing graphene-like band intraband interaction, emerging at the zero temperature supercooling field associated with the metallic interlayer band.

The phase diagrams of Fig. 5.1 provide a background against which future experimental

data concerning superconductivity on GICs should be interpreted. If future measurements of superconducting in-plane critical fields in GICs find two low-temperature first-order transitions, this would imply that both the graphene-like band and the metallic interlayer band participate in the superconducting phase [18, 19, 20, 21, 22, 23, 24, 25]]. On the other hand, the presence of only one low temperature first-order transition would not, by itself, conclusively disprove a two-band description, in favor of a one-band description [17, 16] since, as we showed in Fig. 5.1(a), both bands can be superconducting even if the in-plane magnetic field *vs*. temperature phase diagram is that of a typical one-band superconductor.

In our study of out-of-plane critical magnetic fields, we addressed the pair propagator real space and temperature dependence of a generic one-band superconducting semi-metal. We found that, due to the vanishing of the semi-metallic density of states at the Fermi energy, the pair propagator of a superconductor with a semi-metallic band decays faster than that of a superconductor with a metallic band. Additionally, we found that that the zero field band gap solution does not have solution for weak intraband interaction, that is, as expected, there is a critical intraband interaction in order for a superconducting phase to be present in a system with a semi-metallic density of states.

Furthermore, we studied the superconducting upper critical field *vs.* temperature phase diagram, and found a h_c curve with positive curvature in contrast with the negative curvature of a parabolic curve, typical of a phase diagram of a one-band metallic superconductor.

A similar study can carried out done in the case of a graphene-like band. Despite the more complicated graphene band structure, which includes two different, not isotropic, bands, we believe that, due to the semi-metallic density of states of the graphene band, we will obtain, qualitatively, the same results as the ones of a isotropic semi-metal band. We plan to execute this task, along with a similar study for GICs, as future work, thus making a broader study on critical magnetic fields in superconductors with a semi-metallic band, and in particular with a graphene-like band.

Bibliography

[1] Andre K. Geim and Philip Kim. Carbon Wonderland. *Scientific American*, 298(4):90–97, 2008.

[2] A. K. Geim. Graphene: status and prospects. *Science*, 324(5934):1530–1534, June 2009.

[3] Hubert B. Heersche, Pablo Jarillo-Herrero, Jeroen B. Oostinga, Lieven M. K. Vandersypen, and Alberto F. Morpurgo. Bipolar supercurrent in graphene. *Nature*, 446(7131):56–59, March 2007.

[4] Hubert B. Heersche, Pablo Jarillo-Herrero, Jeroen B. Oostinga, Lieven M. K. Vandersypen, and Alberto F. Morpurgo. Induced superconductivity in graphene. *Solid State Commun.*, 143(1):72–76, July 2007.

[5] N. B. Kopnin and E. B. Sonin. BCS Superconductivity of Dirac Electrons in Graphene Layers. *Phys. Rev. Lett.*, 100:246808, Jun 2008.

[6] N. D. Mermin. Absence of ordering in certain classical systems. *J. Math. Phys.*, 8(5):1061–1064, 1967.

[7] N. D. Mermin and H. Wagner. Absence of Ferromagnetism or Antiferromagnetism in One- or Two-Dimensional Isotropic Heisenberg Models. *Phys. Rev. Lett.*, 17:1133–1136, Nov 1966.

[8] H. le Sueur, P. Joyez, H. Pothier, C. Urbina, and D. Esteve. Phase Controlled Superconducting Proximity Effect Probed by Tunneling Spectroscopy. *Phys. Rev. Lett.*, 100:197002, May 2008.

[9] A. J. Leggett. Number-Phase Fluctuations in Two-Band Superconductors. *Prog. Theor. Phys.*, 36(5):901–930, 1966.

[10] D. F. Agterberg, Eugene Demler, and B. Janko. Josephson effects between multigap and single-gap superconductors. *Phys. Rev. B*, 66:214507, Dec 2002.

[11] Philip J. W. Moll, Xiyu Zhu, Peng Cheng, Hai-Hu Wen, and Bertram Batlogg. Intrinsic Josephson junctions in the iron-based multi-band superconductor ($V_2Sr_4O_6$) Fe_2As_2. *Nature Phys.*, 10(9):644–647, 2014.

[12] N. B. Hannay, T. H. Geballe, B. T. Matthias, K. Andres, P. Schmidt, and D. MacNair. Superconductivity in Graphitic Compounds. *Phys. Rev. Lett.*, 14:225–226, Feb 1965.

[13] Mike Sutherland, Nicolas Doiron-Leyraud, Louis Taillefer, Thomas Weller, Mark Ellerby, and S. S. Saxena. Bulk evidence for single-gap s-wave superconductivity in the intercalated graphite superconductor C 6 Yb. *Phys. Rev. Lett.*, 98(6):067003, Feb 2007.

[14] Nicolas Emery, Claire Hérold, Jean-François Marêché, and Philippe Lagrange. Synthesis and superconducting properties of CaC6. *Sci. and Technol. of Adv. Mater.*, 9(4):044102, January 2008.

[15] Thomas E. Weller, Mark Ellerby, Siddharth S. Saxena, Robert P. Smith, and Neal T. Skipper. Superconductivity in the intercalated graphite compounds C_6Yb and C_6Ca. *Nature Phys.*, 1(1):39–41, 2005.

[16] K. Sugawara, T. Sato, and T. Takahashi. Fermi-surface-dependent superconducting gap in C_6Ca. *Nature Phys.*, 5(1):40–43, 2009.

[17] T. Valla, J. Camacho, Z.-H. Pan, A. V. Fedorov, A. C. Walters, C. A. Howard, and M. Ellerby. Anisotropic Electron-Phonon Coupling and Dynamical Nesting on the Graphene Sheets in Superconducting C_6Ca using Angle-Resolved Photoemission Spectroscopy. *Phys. Rev. Lett.*, 102:107007, Mar 2009.

[18] Gianni Profeta, Matteo Calandra, and Francesco Mauri. Phonon-mediated superconductivity in graphene by lithium deposition. *Nature Phys.*, 8(2):131–134, 2012.

[19] Matteo Calandra and Francesco Mauri. Theoretical Explanation of Superconductivity in C_6Ca. *Phys. Rev. Lett.*, 95:237002, Nov 2005.

[20] A. Sanna, G. Profeta, A. Floris, A. Marini, E. K. U. Gross, and S. Massidda. Anisotropic gap of superconducting CaC_6: A first-principles density functional calculation. *Phys. Rev. B*, 75:020511, Jan 2007.

[21] Lilia Boeri, Giovanni B. Bachelet, Matteo Giantomassi, and Ole K. Andersen. Electron-phonon interaction in graphite intercalation compounds. *Phys. Rev. B*, 76:064510, Aug 2007.

[22] J. S. Kim, R. K. Kremer, L. Boeri, and F. S. Razavi. Specific Heat of the Ca-Intercalated Graphite Superconductor CaC_6. *Phys. Rev. Lett.*, 96:217002, Jun 2006.

[23] G. Lamura, M. Aurino, G. Cifariello, E. Di Gennaro, A. Andreone, N. Emery, C. Hérold, J.-F. Marêché, and P. Lagrange. Experimental Evidence of *s*-Wave Superconductivity in Bulk CaC_6. *Phys. Rev. Lett.*, 96:107008, Mar 2006.

[24] N. Bergeal, V. Dubost, Y. Noat, W. Sacks, D. Roditchev, N. Emery, C. Hérold, J-F. Marêché, P. Lagrange, and G. Loupias. Scanning Tunneling Spectroscopy on the Novel Superconductor CaC_6. *Phys. Rev. Lett.*, 97:077003, Aug 2006.

[25] R. S. Gonnelli, D. Daghero, D. Delaude, M. Tortello, G. A. Ummarino, V. A. Stepanov, J. S. Kim, R. K. Kremer, A. Sanna, G. Profeta, and S. Massidda. Evidence for Gap Anisotropy in CaC_6 from Directional Point-Contact Spectroscopy. *Phys. Rev. Lett.*, 100:207004, May 2008.

[26] S.-L. Yang, J. A. Sobota, C. A. Howard, C. J. Pickard, Makoto Hashimoto, D. H. Lu, S.-K. Mo, P. S. Kirchmann, and Z.-X. Shen. Superconducting graphene sheets in CaC_6 enabled by phonon-mediated interband interactions. *Nat. Commun.*, 5, 2014.

[27] J. S. Kim, L. Boeri, J. R. O'Brien, F. S. Razavi, and R. K. Kremer. Superconductivity in Heavy Alkaline-Earth Intercalated Graphites. *Phys. Rev. Lett.*, 99:027001, Jul 2007.

[28] Yasuhiro Iye and Sei-ichi Tanuma. Superconductivity of graphite intercalation compounds with alkali-metal amalgams. *Phys. Rev. B*, 25:4583–4592, Apr 1982.

[29] K. Maki and T. Tsuneto. Pauli Paramagnetism and Superconducting State. *Prog. Theor. Phys.*, 31(6):945, 1964.

[30] Hiroshi Shimahara. Fulde-Ferrell state in quasi-two-dimensional superconductors. *Phys. Rev. B*, 50:12760–12765, Nov 1994.

[31] R. G. Dias and J. A. Silva. Huge metastability in high-T_c superconductors induced by parallel magnetic field. *Phys. Rev. B*, 67:092511, Mar 2003.

[32] H. Kamerlingh Onnes. The superconductivity of mercury. *Comm. Phys. Lab. Univ. Leiden*, 122:124, 1911.

[33] Peter Hirschfeld. *Advanced Solid State Physics Lecture Notes*, 2013.

[34] John Bardeen, Leon N. Cooper, and J. Robert Schrieffer. Theory of superconductivity. *Physical Review*, 108(5):1175, 1957.

[35] JamesWilliam Rohlf. *Modern physics from α to Z^0*. Wiley-VCH, 1994.

[36] Frank J. Blatt. *Modern physics*. McGraw-Hill, 1992.

[37] R. G. Dias. Zeeman splitting in multiple-band superconductors. *Phys. Rev. B*, 72:012505, Jul 2005.

[38] H. Suhl, B. T. Matthias, and L. R. Walker. Bardeen-Cooper-Schrieffer Theory of Superconductivity in the Case of Overlapping Bands. *Phys. Rev. Lett.*, 3:552–554, Dec 1959.

[39] A. M. Marques, R. G. Dias, M. A. N. Araujo, and F. D. R. Santos. In-plane magnetic field vs. temperature phase diagram of a quasi-2D frustrated multiband superconductor. *Supercond. Sci. Technol.*, 28(4):045021, 2015.

[40] A. H. Castro Neto, F. Guinea, N. M. R. Peres, K. S. Novoselov, and A. K. Geim. The electronic properties of graphene. *Rev. Mod. Phys.*, 81:109–162, Jan 2009.

[41] Riichiro Saito, Gene Dresselhaus, Mildred S Dresselhaus, et al. *Physical properties of carbon nanotubes*, volume 35. World Scientific, 1998.

[42] B. Gharekhanlou and S. Khorasani. *An overview of tight-binding method for two-dimensional carbon structures*. Hauppauge, NY, USA: Nova Science Publishers, 2011.

[43] Jean-Noël Fuchs and Mark Oliver Goerbig. Introduction to the physical properties of graphene. *Lecture Notes*, 2008.

[44] Bruno Uchoa and A. H. Castro Neto. Superconducting States of Pure and Doped Graphene. *Phys. Rev. Lett.*, 98:146801, Apr 2007.

[45] Eduardo V. Castro, María P. López-Sancho, and María A. H. Vozmediano. Pinning and switching of magnetic moments in bilayer graphene. *New J. Phys.*, 11(9):095017, 2009.

[46] L. P. Gorkov. The critical supercooling field in superconductivity theory. *JEPT*, 10(3):593–599, 1960.

[47] A. A. Abrikosov, L. P. Gorkov, and I. E. Dzyaloshinski. *Methods of Quantum Field Theory in Statistical Physics*. Courier Corporation, 1975.

[48] C. C. Sung. Magnetic Properties of Type-II Superconductors in the Two-Bandand Model. *Phys. Rev.*, 187(2), November 1969.

[49] A. K. Rajagopal and R. Vasudevan. De Haas–Van Alphen oscillations in the critical temperature of type-II superconductors. *Phys. Lett.*, 23, 1966.

[50] Gerald D. Mahan. *Many-particle physics*. Springer Science & Business Media, 2013.